MODELING OF THE ELECTROCHEMICAL CONVERSION OF CO_2 IN MICROFLUIDIC REACTORS

BY

KUNNA WU

DISSERTATION

Submitted in partial fulfillment of the requirements
for the degree of Doctor of Philosophy in Chemical Engineering
in the Graduate College of the
University of Illinois at Urbana-Champaign,
in the program jointly administered with the
National University of Singapore, 2015

Urbana, Illinois

Doctoral Committee:

Associate Professor Jianwen Jiang, Chair, National University of Singapore
Professor Paul J A Kenis, Co-Chair, Director of Research
Professor Iftekhar Karimi, Co-Director of Research, National University of Singapore
Professor Hong Yang
Associate Professor Saif Khan, National University of Singapore
Associate Professor Karl Erik Birgersson, National University of Singapore
Professor Jonathan Higdon

ABSTRACT

Today's world faces immense challenges associated with meeting its energy needs, due to its current dependence on fossil fuels. At the same time, the world faces the threat of global climate change linked to CO_2 emissions. Indeed, global energy consumption is expected to double in the next 50 years. This accelerates the depletion of conventional fossil fuels and leads to a steady increase in CO_2 emission. Globally, CO_2 emission through the combustion of fossil fuels has increased by about 1.6 times between 1990 (the Kyoto Protocol reference year) and 2013, with approximately 9.9 GtC added to the atmosphere in 2013. Taken together, the dual challenges of finding alternative energy sources and curbing CO_2 emissions are very daunting. When it is powered by carbon-neutral electricity sources, the electrochemical conversion of CO_2 into value-added chemicals offers an economically viable route to recycle CO_2 towards reducing CO_2 emissions and reducing dependence on fossil fuels.

The majority of prior studies on the electrochemical conversion of CO_2 are experimental in nature, focused on unravelling the mechanisms of known catalysts. As an alternative approach to the laborious experiments, first-principles modeling of the electrochemical reactors can complement the current experimental work by elucidating the complex transport and electrochemistry, particularly in the porous electrodes, and help in the design and optimization of such reactors. Currently, there is a lack of detailed modeling for the aqueous electrochemical reduction of CO_2 in a microfluidic reactor, which has been demonstrated experimentally to be an effective reactor and a versatile analytical tool.

This thesis focuses on developing a mathematical modeling framework for the electrochemical conversion of CO_2 to CO in microfluidic reactors. Conversion of CO_2 into

CO is attractive due to the versatility of CO (with H_2) as a feedstock for the production of a variety of products including liquid hydrocarbon fuels. A full model that takes into account of all the significant physics and electrochemistry in the cell, including the transport of species and charges, momentum and mass conservations, and electrochemical reactions, is first formulated. The full model that comprises of a system of coupled partial differential equations is solved using finite element method. It is then calibrated and validated using experimental data obtained for various inlet flow rates and compositions. Parametric studies for various design and operating variables are subsequently performed using the validated model. To reduce the computational time, yet preserve the geometric resolution and leading order behavior of the cell, narrow-gap approximation and scaling arguments are invoked which allow for significant reduction in the mathematical complexity of the full model and eventually approximate analytical solutions. The unit cell models are then extended to stack models for simulation and analysis of the electrochemical reduction of CO_2 in a microfluidic cell stack.

ACKNOWLEDGEMENTS

First, it is my great pleasure to extend my most sincere and deepest gratitude to my supervisors, Prof. Paul Kenis and Prof. Iftekhar Karimi for the inspiration, guidance and support. Thanks to Prof. Kenis and Prof. Karimi for mentoring me through my PhD candidature. This thesis would not have been possible without them.

I would like to convey my special thanks to Dr. Karl Erik Birgersson for his willingness to share his knowledge and expertise that are of significant relevance to this work. I am very grateful for all the open and stimulating discussions, and really appreciate all his contribution of time and ideas.

I am appreciative of my thesis examination committee, Prof. Hong Yang, Dr. Saif Khan, and Dr. Jianwen Jiang for providing me critical review and insightful comments. I am also thankful to my thesis advisory committee, Prof. Hong Yang, Prof. Jonathan Higdon, Dr. Erik Birgersson and Dr. Saif Khan for the valuable feedback provided during each committee meeting.

I would like to acknowledge the Agency for Science, Technology and Research (A*STAR, Singapore) for providing funding for the NUS-UIUC Joint Ph.D. fellowship. I would also like to thank the National University of Singapore and University of Illinois at Urbana-Champaign for providing this research opportunity.

I am also very grateful for the generous help and advice given by my co-workers throughout my candidature. Special thanks to Dr. Michael Thomson and Mr. Byoungsu Kim for providing the experimental results.

Last but not least, I would like to extend my deepest gratitude to my parents, my sister and all my friends for the encouragement and emotional support throughout my entire candidature.

TABLE OF CONTENTS

LIST OF SYMBOLS

a_i	specific surface (ratio of reaction surface of the active sites to catalyst layer volume), 1/m
C_i	concentration of species *i*, mol/m^3
Conv	conversion of CO_2 per pass
D_{ij}	multicomponent diffusion coefficients, m^2/s
e	unit normal vector
err	error
E_i	reversible potential of the half-cell corresponding to formation of species *i*, V
F	Faradaic constant, 96485 C/mol
FE	Faradaic efficiency
g	acceleration due to gravity, m/s^2
H	height, m
i	current density, A/m^2
i_i	transfer current density corresponding to the formation of species *i*, A/m^2
$i_{\mathrm{i,ref}}$	exchange current density corresponding to the formation of species *i*, A/m^2
I	identity tensor
L	channel length, m
M_i	molecular mass of species *i*, kg/mol
$\mathbf{n}_i$	mass flux of species *i*, kg/(m^2·s)
N	number of species
O	order of magnitude

p	pressure of gas, Pa
Q	mass source term, kg/(m^3·s)
r_f	carbon fiber radius in the diffusion layer, m
R	universal gas constant, 8.314 J/mol·K
R_i	reaction rate of species *i* in the electrochemical reaction, kg/(m^3·s)
RMSE	root mean squared error/difference
S	current source term, A/m^3
T	temperature, K
$\mathbf{u}$	velocity, m/s
u	velocity in the x direction / streamwise direction, m/s
$U_{\mathrm{g,in}}$	average normal inflow velocity, m/s
v	velocity along the y direction / normal direction, m/s
v_i	diffusion volume of molecule *i*, used in the correlation by Fuller, Schettler, and Giddings
V	applied potential, V
V_{anod}	applied potential at the anode, V
V_i	molar volume of species i, m^3/mol
V_{cath}	applied potential at the cathode, V
V_{stack}	applied potential across a cell stack, V
W	width, m
x_i	molar fraction of species *i*

Greek

α	fitting parameter for through-plane diffusion in the Tomadakis-Sotirchos

	model
α_i	charge transfer coefficient of the half-cell corresponding to the formation of species *i*
ε	porosity of the gas diffusion layer or catalyst layer
ε_p	percolation threshold porosity, used in the Tomadakis-Sotirchos model
η_i	overpotential of the formation reaction species *i* , V
κ	permeability of the gas diffusion layer or catalyst layer, m^2
Λ	Damkohler number, dimensionless constant for ratio of the mass flux of electrochemical reaction to the convective flow
λ	eigenvalues
μ	dynamic viscosity, kg/m·s
ρ	density of gas, kg/m^3
σ	electric conductivity, S/m
ϕ	electric potential
ω_i	mass fraction of species *i*
Ω	modified Damkohler number, modified the dimensionless constant Damkohler by a length scale

Subscript

anod	at the anode
cath	at the cathode
cell	for the whole cell
cl	catalyst layer
cl_l	liquid phase in the catalyst layer

cl_s	solid phase in the catalyst layer
elec	at the electrolyte
exit	at the exit
f	carbon fiber
gbot	lower portion of the gas channel
gdl	gas diffusion layer
gext	extended length of the gas channel
gtop	upper portion of the gas channel
i	index for individual species or individual cell in the stack
in	at the inlet or in the feed
j	index for individual species or individual cell in the stack
k	experiment number
l	liquid phase
p	percolation threshold
ref	reference
s	solid phase
sat	saturated
stack	for the cell stack
total	total
x	along the flow direction
y	along the height of the cell direction

Superscript

eff	effective

exp	experimental
num	numerical
T	transpose

CHAPTER 1

INTRODUCTION

1.1 Overview

Today's world faces immense challenges in meeting its energy demand. As fossil fuels are expected to continue to supply almost 80% of world energy use through 2040 [1], the increase in global energy consumption accelerates the depletion of fossil fuels and leads to a steady increase in carbon dioxide (CO_2) emissions. Global CO_2 emissions from the combustion of fossil fuels have increased by about 60% over 1990 (the Kyoto Protocol reference year), with approximately 9.9 GtC added to the atmosphere in 2013.[2] This drastic rise in CO_2 emissions has caused much concern, and has been universally deemed as the main cause of global warming. Several studies indicate that CO_2 emissions must be reduced significantly, by as much as 50% of those in 1990, by 2050 to limit the potential effects of climate change.[3-6] Such pressure has pushed for research and development in technologies for carbon capture, sequestration and utilization.

Carbon capture and sequestration (CCS) has been the focus of intense research in the past decade, with the motivation to mitigate CO_2 emissions to the atmosphere. Such processes include the capture of CO_2 from sources such as fossil fuel based power plants, and the subsequent transport of the captured CO_2 for long-term storage underground or in ocean.[7] Overall strategies for CCS do not merely involve trapping CO_2 from point source, but also include the purification of CO_2, compression for ease of transportation, and transportation of compressed CO_2 for long-term storage. These processes required added energy input that may release CO_2. Additionally, the long-term storage of CO_2 has yet to be

fully realized. The storage of CO_2 in the ocean is connected with negative impacts on the oceanic flora and fauna and prohibited according to international agreements (OSPAR, London Convention).[8] There is also a school of thought believing that geological storage does not resolve the problem permanently, just shifts that from the atmosphere to somewhere else.[9-11]

In view of such limitations in CCS, utilization of CO_2 is increasingly being explored as an alternative to geological sequestration as it also has the potential advantage of generating new revenue streams. Considerable research is underway in several directions to advance the promise of processes that utilize CO_2. Essentially, three pathways exist for CO_2 utilization: (1) as a storage medium for renewable energy via conversion into fuels; (2) as a feedstock for the production of various chemicals such as urea, cyclic carbonates and salicylic acid; and (3) non-conversion use of CO_2 as a solvent, heat transfer fluid or working fluid.[9, 12, 13] Conversion of CO_2 into fuels is especially attractive as it has the potential advantage of addressing the dual challenges of reducing dependence on fossil fuels and curbing CO_2 emission.

There are different possible routes towards fuel production from CO_2 conversion such as catalytic hydrogenation and dry reforming. In terms of direct utilization of renewable energy so that the process can be utilized as a storage mechanism for renewable energy, three typical approaches are:

(1) Thermochemical conversion using concentrated sunlight [14, 15]

Nonstoichiometric oxides such as cerium oxide are partially reduced at high temperature (1873 K for cerium oxide), releasing O_2 under concentrated solar radiation, and then react with CO_2 and H_2 at lower temperature. During this process, CO_2 is reduced to CO. A major challenge in the application of thermochemical

conversion of CO_2 is the high investment cost associated with the focusing lenses for sunlight and high-temperature reactors.

(2) Photocatalytic conversion[16-18]

The primary steps of photocatalytic reduction of CO_2 are absorption of light photons in a photocatalyst material, and subsequent conversion of these photons into electron-hole pairs, which then have to be spatially separated to drive chemical oxidation and reduction half-reactions at the semiconductor-electrolyte interface. The overall results of this process depend on the reaction conditions, such as the incident/absorbing light intensity from the sun or a simulated solar light source.

(3) Electrochemical conversion[19-21]

Following the concept of water electrolysis, a large number of studies have examined the use of electrocatalysts to reduce CO_2. A wide range of products starting from carbon monoxide (CO) to more complex pure and oxygenated hydrocarbons of high energy content can be directly synthesized. In general, the process involves the reduction of CO_2 by applying a voltage between two electrodes, a voltage difference that is greater than that necessitated by thermodynamics.

This thesis focuses on the electrochemical conversion of CO_2 for its several advantages: (1) the process is controllable by electrode potentials; (2) the supporting electrolytes can be fully recycled so that the overall chemical consumption can be minimized to simply water; (3) the electricity used to drive the process can be obtained without generating any new CO_2 from renewable sources such as solar, wind, hydro-electric, geothermal, tidal and thermoelectric processes; and (4) the electrochemical reaction systems are compact, modular, can be operated on-demand, and be scaled to large volume conversion.[22]

1.2 Electrochemical Conversion of CO_2

The electrochemical conversion of CO_2 relies on an electrochemical reactor, often called an electrolyzer, which balances electro-catalytic reduction and oxidation reactions. A schematic diagram for this process is shown on the left of Figure 1.1. CO_2 captured is fed into the cathode side of the reactor and reduced into fuels such as carbon monoxide (CO)[23-26], formic acid/formate[19, 27-29], methane[30-32], ethylene[33-37], and alcohols[38-40], while water on the anode side is oxidized into oxygen (O_2). As the process is endergonic, unlike in the case of fuel cell, a potential must be applied between the anode and cathode. The theoretical potential necessary for the reaction is the difference between the standard potentials for both the anode and cathode reactions. The standard reduction potentials of the common electrode reactions are shown on the right of Figure 1.1.

To explore the electrochemical conversion of CO_2 as a means of storage for renewable energy, the electrochemical process can be tied to renewable power sources in several ways: (1) direct use of electricity produced by a renewable source to power the electrochemical reactor in a continuous fashion; (2) transient process that only utilizes excess electricity produced by a renewable source in off-peak time when the demand of electricity is much lower than that produced; and (3) co-operation with a fuel cell to (a) store excess electrical energy from a renewable source in chemical form in off-peak time and (b) convert the chemicals back to electricity when the demand is high again. Storing electrical energy from intermittent power sources in chemical form when the demand for electricity is low has the potential to improve the overall process economics for renewable energy sources and thereby enable wider penetration of renewable technology.

1.3 Challenges and Opportunities

An economically viable electrochemical technology requires optimization of four key parameters: (1) current density – a measure of the rate of conversion; (2) Faradaic efficiency – a measure of the selectivity of the process for a given product; (3) energetic efficiency or specific electricity consumption – a measure of the overall energy utilization towards the desired product; and (4) electrode lifetime. Prior reports and reviews have provided an excellent overview of possible products of electrochemical CO_2 reduction at a wide range of current densities, Faradaic efficiency and energetic efficiency for the desired product.[20, 21, 41, 42] Despite the various advances in CO_2 electrochemical reduction technology, several technical challenges remain:

(1) Search for better catalyst to ensure catalyst activity and catalyst stability/durability

The potential needed for CO_2 electrochemical reduction is normally much higher than the theoretical potential required. This indicates a great opportunity for improvement in catalyst activity. The active electrode/catalyst surface can gradually become covered by reaction intermediates and by-products (such as carbon films and poisonous species), blocking and poisoning the catalysts' active sites and leading to rapid catalytic activity degradation.[43] In the literature, the normally reported stability tests are only in the region of under 100 hours, while long-term tests have yet to be done.

(2) Improvement on fundamental understanding

The literature contains attempts to fundamentally understand the CO_2 reduction process through experimental efforts and theoretical modeling approaches, with the goal to predict or understand catalyst activity, and to aid new catalyst design and

optimization. However, work in this area is still very limited, mainly focused on unravelling the mechanisms of the known catalysts.

(3) Optimization of electrode/reactor and system design for practical applications

Based on our experience, CO_2 electrolysis is more sensitive to the structure and composition of the electrodes than an identical cell operated as a fuel cell. Further efforts should focus on assessing to what extent the physical properties of the gas diffusion layers impact on the effective gas-liquid phase separation while facilitating the transport of reactants and products. The scale-up of the electrochemical reduction of CO_2 for practical applications is also a necessary step toward the success of this technology.[22] To date, only a few attempts have been carried out to study scale-up of the process.

An effective approach to address the above challenges is to develop a mathematical framework for the electrochemical conversion of CO_2. Mathematical modeling intrinsically can save time and cost as numerical experiments can be carried out significantly faster and cheaper as compared to practical experiments. Additionally, there are several other advantages of mathematical modeling:

(1) It helps to build a fundamental understanding of the series of intrinsically coupled physicochemical processes, which include mass, species, momentum, charge transport, and multiple electrochemical reactions.

(2) Modeling is an efficient way to perform design optimization at small scale such as the catalyst layer where experimental testing is either difficult or impossible due to the small scale. Ultimately, it can intensify innovation.

(3) Mathematical modeling provides a more comprehensive approach for investigating the parameters that affect the performance of the single cell and/or cell stack systems.

(4) Mathematical modeling can also contribute towards holistic optimization of cell design, material management and controls of operation.

1.4 Research Objectives

The focus of this study is to develop a mathematical framework for the modeling of the electrochemical conversion of CO_2 in microfluidic reactors. Microfluidic reactors are selected as the platform because it has been demonstrated to be an effective reactor and a versatile analytical tool for the electrochemical reduction of CO_2 in several experimental studies [19, 44-46]. Conversion of CO_2 to CO is considered, because rather than the direct conversion to liquid fuels, the strategic approach from kinetic consideration is to convert CO_2 into CO which combines with H_2 to yield synthesis gas (syngas), and then to use proven technologies such as the Fischer-Tropsch process to convert the syngas to liquid fuels.[47] Furthermore, conversion of CO_2 to CO only produces gaseous products, which is much easier to recover as compared to reduction to other liquid fuels such as methanol which requires additional energy input for recovery using distillation.

Modeling of the electrochemical conversion of CO_2 to CO in microfluidic reactors is very complicated and challenging. First, there is not prior research on the mathematical modeling of such system. Second, the system is very complex because of two main inherent characteristics: multiphysics and multiscale. There are multiple coupled transport phenomena, comprising of the conservation of mass, momentum, species and charge. The system also involves multiple length scales: the functional layers in the cell have length scales of around O (10^{-6} – 10^{-4}) m, while the cell itself has a length scale of O (10^{0} – 10^{1}) m. While

multiphysics leads to multitude of dependent variables that needs to be solved for, multiscale requires to resolve all the length scales, resulting in a large number of degrees of freedoms. This problem gets even more complicated and challenging when the detailed transport model is applied to cell stacks comprising of tens or hundreds of cells. Computational cost will also increase tremendously if unit cell model of the same level of complexity and resolution is applied as the building block in the cell stack modeling. There is a need to search for a balance between model complexity and computational efficiency.

To address the challenges, this research aims to:

(1) Perform literature review on the modeling of similar systems such as modeling of CO_2 electrolyzers or modeling of microfluidic fuel cells which are either similar in the electrochemistry involved or the reactors used but not both. Based on the literature review, information such as the basis of modeling (black box model vs physical model), dimensionality of the model and processes to be included in the model could be derived.

(2) Develop a mathematical modeling framework while balancing model complexity and computational efficiency by:

   (i) Starting with a detailed model for the electrochemical conversion of CO_2 in a microfluidic cell, to capture all the significant physics and electrochemistry in the cell including the transport of species and charges, momentum and mass conservation and electrochemical reaction kinetics.

   (ii) Calibrating the kinetic parameters in the model and validating the model to ensure the credibility of the simulation results obtained from the model in further study.

(iii) Performing parametric study using the validated model to study important factors that may affect the performance of the reactor.

(iv) Developing a reduced model for the electrochemical conversion of CO_2 in a microfluidic cell that leads to significant reduction in computational cost and efficiency while preserving the geometry and leading order physics.

(v) Extending the developed unit cell models to model cell stacks comprising of *n*-cell for electrochemical conversion of CO_2. Cell stack modeling is essential to test the scalability of the system and the model. It will enable future analysis of the practical applicability of the system.

1.5 Organization of Thesis

In addition to this introductory chapter, which motivates the aim of this research, this thesis is comprised of another seven chapters.

Chapter 2 provides a detailed perspective of the fields of modeling of electrochemical conversion of CO_2 and modeling of microfluidic fuel cell. A review on the various mathematical models in the literature is given, and serves as the context for the contributions reported in this thesis.

Chapter 3 is the core chapter of this thesis. It details the mathematical formulation of the electrochemical reduction of CO_2 in a microfluidic cell. The steady state and isothermal model developed accounts for the transport of species and charges, momentum and charge conservation, and electrochemical reaction kinetics. This full model forms the backbone to this thesis.

Due to incomplete knowledge of the underlying electrochemical catalytic reactions and excessive complexity of accommodating reaction mechanisms into the fluidic flow model, electrochemical kinetic parameters, in this case the charge transfer coefficients and the exchange current densities need to be calibrated based on experimental results. Details for parameter estimation are discussed in Chapter 4. Results of the model validation are also discussed to ensure credibility of the model. Validity of the 2D model assumption is also verified.

In Chapter 5, the use of the model for parametric study is demonstrated. The effects of several operating and design parameters, such as applied cell potential, feed CO_2 composition, feed gas flow rate, channel length and electrode porosity, on the performance of the microfluidic cell are discussed.

Owing to the highly coupled partial differential equations of a typical microfluidic electrochemical flow model, the detailed model presented in Chapter 3 need to be solved numerically, and can entail significant computational cost and/or complexity. In Chapter 6, the full model presented in Chapter 3 is reduced based on scaling arguments. A reduced model that preserves geometry and leading order physics is developed. Approximate analytical solutions of the reduced model are derived and verified with the numerical solution of the full model.

The fast and efficient unit cell model obtained can then be utilized to build a model for cell stacks. In Chapter 7, the unit cell models presented in Chapter 3 and Chapter 6 are extended to model cell stacks. The reduced stack model based on approximate analytical solutions is verified with the full model. Extensions to include non-uniformity such as non-uniform feed flow are also discussed.

Chapter 8 is the concluding chapter of this thesis work. It summarizes all the work discussed in this thesis and recommends possible future directions.

1.6 Figure

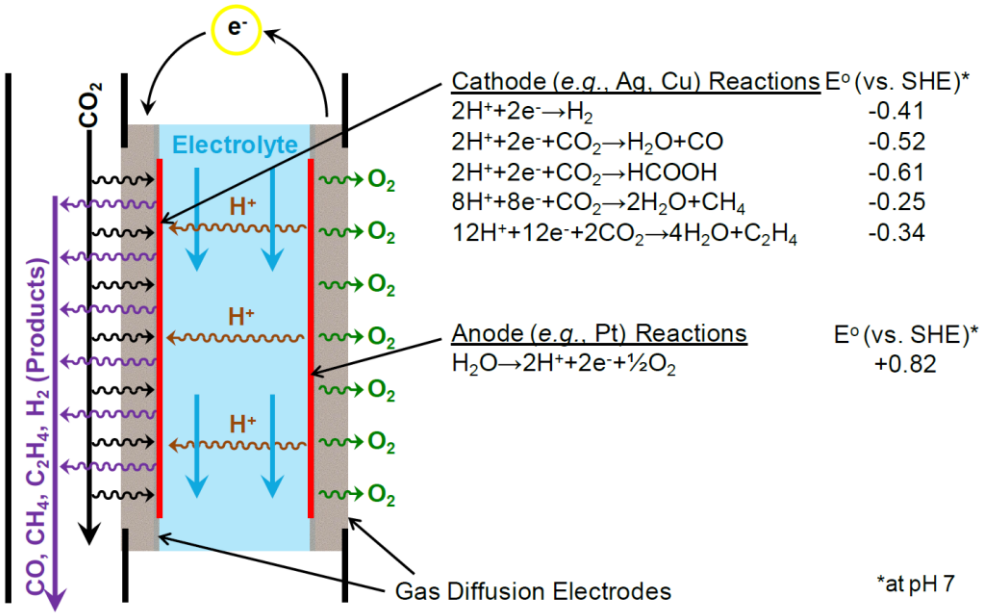

Figure 1.1. (Left) Schematic of an electrochemical reactor for CO_2 reduction, and (Right) Standard reduction potentials for the common cathode and anode reactions. [48]

CHAPTER 2

LITERATURE REVIEW

2.1 Introduction

This chapter provides an overview of the current development in the electrochemical reduction of CO_2, highlights the lack of mathematical modeling for the electrochemical reduction of CO_2 in a microfluidic cell. In order to develop a mathematical model for the electrochemical reduction of CO_2 in a microfluidic cell, a review of the available models for other types of reactors used for the electrochemical reduction of CO_2 (CO_2 electrolyzers), especially solid oxide electrolysis cell (SOEC), is presented. As the microfluidic flow cell of our interest is in fact a microfluidic fuel cell (MFC) operated in reverse direction, models for MFCs are also discussed.

2.2 Overview of the Electrochemical Reduction of CO_2

The electrochemical conversion of CO_2 into useful products by utilizing a renewable or carbon neutral electricity source, such as solar, wind, hydroelectric, geothermal, tidal and thermoelectric power, is receiving increased attention. Several electrochemical flow reactor designs have been reported in the literature, such as an electrolytic cell with a separator[26], solid oxide electrolysis cells[49-52], and microfluidic electrolytic cells[19, 44, 45]. A variety of products, such as carbon monoxide (CO)[23-26], formic acid/formate[19, 27-29], methane[30-32], ethylene[33-37], and alcohols[38-40], can be obtained from the electrochemical process. The product selectivity depends on the cathode catalyst, applied cell potential, and the electrolyte composition. A variety of catalysts, including various metals[29, 53-55], metal oxides[56], metal organic frameworks[57], and organometallic compounds[46]

have been tested. For recent developments in reactor design, catalyst selection, and electrode structure for the electrochemical reduction of CO_2, the reader is referred to the review articles by Jhong et al.[20] and Lim et al.[21].

The majority of prior studies on the electrochemical conversion of CO_2 have been experimental in nature. They have explored different types of electrodes and catalysts to improve performance, and to unravel the possible electro-reduction mechanisms.[20, 21, 58] Mathematical modeling of the electrochemical reactors can complement the experimental work reported to date by elucidating the complex interplay between transport and electrochemistry, particularly in porous electrodes. The results of such studies can help in the design and optimization of these electrochemical reactors. To date only few modeling studies on the electrolysis of CO_2, and hardly any studies for this process taking place in a microfluidic flow cell have been reported.

2.3 Modeling of CO_2 Electrolyzers

Several modeling studies on the electrochemical reduction of CO_2 will be discussed in this section.

Li & Oloman[59] presented a crude cathode model for the electrochemical reduction of CO_2 to potassium formate in a continuous "trickle-bed" reactor. By treating the cathode as a plug flow reactor, the model divided the cathode into a number of increments of height and calculates the overall performance at steady-state by forward differencing in an Excel spreadsheet. Their model only involved relationships for the stoichiometry, equilibria and kinetics of the electrochemical reactions. The numerical results solved using this crude model agreed poorly with the experimental results, with a regression coefficient of 0.64 and maximum error of about 20%.

Delacourt & Newman[60] proposed a detailed model for the reduction of CO_2 to CO in a cell similar to a proton-exchange-membrane fuel cell, but with an additional aqueous buffer layer. Equilibrated reactions were assumed in the model. Their model predicted the experimental data pretty well, but only at current densities that are smaller than 10 mA/cm^2.

The majority of prior studies on mathematical modeling of CO_2 electrolysis pertained to the development of models for SOECs.

Shi and co-workers[61] developed a one-dimensional (1D) elementary reaction based model of an SOEC operating with CO/CO_2 mixture gas based on button cell geometry. The model incorporated elementary heterogeneous reactions, electrochemical kinetics, electrode microstructure, mass transport and charge transfer within the electrode. From the same research group, Li and his co-workers[62] presented a similar model for the co-electrolysis of CO_2/H_2O in a SOEC. The effects of microstructure and cathode thickness were investigated through similar numerical analysis in their later study.[63] They also analyzed the effects of charge and mass transport in a subsequently study.[64] Li and co-workers[65] also extended their work to study methane production characteristics, and hypothesized about pathways that led to methane formation. All the models developed in this research group as discussed so far are 1D. Luo and co-workers[66] from the same research group developed a two-dimensional (2D) model to analyze the performance and efficiency of H_2O/CO_2 co-electrolysis in a tubular SOEC. The significance of this model lied in the fact that they connected the micro-scale electrode model to the macro-scale cell unit model. The area of the triphase boundary where electrochemical reactions are taking place was calculated using the particle coordinate in binary random packing of spheres together with percolation theory. An approximate analytical model of the electrolysis of CO_2 in SOEC was also developed using perturbation

methods by this research group.[67] The model integrated the rules of Ohmic law, Butler-Volmer equation, theoretical electrolytic voltage and Fick's second law of diffusion.

Ni[68] presented both 1D and 2D models to investigate the performance of CO_2 reduction in a SOEC. The 1D model considered only the electrochemical losses while the 2D model integrated the 1D model to a thermal-fluid model. Modeling of the co-electrolysis of CO_2 and H_2O, taking into account of the global chemistry, was illustrated in another study.[69] The co-electrolysis model quantified the concentration for reverse water-gas-shift (RWGS) reactions to CO production or consumption, along with its dependence on the operating conditions. Subsequently, Ni[70] presented a 2D computational fluidic dynamic (CFD) model to study the combined effects of heat/mass transfer and chemistry/electrochemistry in a SOEC for H_2O/CO_2 co-electrolysis. In addition to RWGS, reversible methanation reaction was also included in the model. The methanation reaction was found to be not favored during co-electrolysis.

Xie & Xue[71] presented a similar CFD modeling approach for syngas production using a button cell geometry. Detailed surface chemistry was incorporated into the multi-transport processes of charge, mass, momentum and energy. Their simulation results led to the conclusion that the surface electrolysis process of CO_2 and H_2O are independent with each other.

Narasimhaiah & Janardhanan[72] presented two different electrochemical models for the reduction of CO_2, with one for the dense electrolyte and electrode interface while the other for the electrode. They developed a modified Butler-Volmer equation of the electrochemical reaction based on multi-step single-electron transfer reactions, and used to account charge transfer in the two models.

Garcia-Gamprubi and co-workers[73] presented a comprehensive numerical tool for the simulation of a solid oxide regenerative fuel cell. Note that they presented a literature review regarding the evaluation of the electrochemical parameters, and concluded that this process was often overlooked in the literature, and where it was mentioned, it was not properly justified in general. They highlighted that overlooking the parameter estimation process does not only greatly diminish the usefulness of the model as a design tool, but also contributes with uncertainty rather than guidance when published in the literature.

In terms of system level analysis, Stempien and co-workers[74] presented a simple thermodynamic model of SOEC system and performed energy and exergy analysis. The simple system consists of a SOEC, heat exchangers and gas separation unit. Subsequently, they extended the system by combining the previous system with power plant under various operating conditions.[75]

2.4 Modeling of Microfluidic Fuel Cells

Numerous modeling studies of MFCs or membraneless micro flow cells have been conducted over the last decade. The advancement of modeling and simulation in MFCs is discussed in this section.

The first computational model for MFCs was developed by Bazylak et al.[76] who considered a T-shaped formic acid/dissolved oxygen microfluidic fuel cell with side-by-side streaming and suggested methods to improve fuel utilization by using tapered electrodes. The transport processes were solved in three-dimension (3D) using a CFD framework coupled with convective/diffusive mass transport and electrochemical reaction rate models for both anode and cathode.

An extended theoretical/computational model was developed by Chang and co-workers[77], included a Butler-Volmer model for the electrochemical kinetics in a Y-shaped formic acid/dissolved oxygen-based cells. It has the capability of predicting complete polarization curves. A similar model for the planar or F-shaped channel was reported by Chen et al.[78] which was complemented by a 2D theoretical model of the cathode kinetics under co-laminar flow.[79] Chen and co-workers[80] also developed a Butler-Volmer model for the MFC using hydrogen peroxide as both fuel can oxidant in mixed media, examining the effects of species transport and geometrical design.

Ahmed and co-workers[81] conducted a numerical simulation study using a 3D steady-state and isothermal model with a trident-shaped micro channel geometry to determine the optimum geometry to enhance the reactant distribution and fuel utilization.

Wang and co-workers[82] worked on a 3D model to compare the flow and heat transfer characteristics of symmetric/asymmetric tree-like branching networks and symmetric/asymmetric (offset) leaf-like branching networks built into heat sinks, leading to the conclusion that asymmetry minimally influenced the tree-like branching network at low branching numbers.

Khabbazi and co-workers[83] conducted a very comprehensive numerical study by developing different 3D numerical models of different microfluidic fuel cells to determine the effect of different modifications which have been implemented in MFCs since its advent. The modifications included the channel geometry aspect ratio and electrode configuration, a third flow between the anolyte and catholyte in the channel, and multiple periodically placed inlets.

Krishnamurthy and co-workers[84] developed a computational model of a microfluidic cell with flow-through porous electrodes. The coupled problem of fluid flow, mass transport and electrochemical kinetics was solved from first principles using the modeling software,

COMSOL Multiphysics. They simulated the catalyst layer as homogeneous media and did not consider its compositions.

Modeling of an air-breathing MFC was presented by Shaegh et al.[85]. Their model assumed a constant oxygen concentration and therefore failed to consider the naturally and forced convective mass transfer resistance in the gas phase. Similar study was conducted by Xuan and co-workers[86], in which they developed a numerical model to predict the transport and reaction patterns of the oxygen electrode and its electrochemical performance under different pH environment for an air-breading reversible MFC. The same research group developed a more detailed mathematical model based on a forced-air-convection MFC.[87] Comprehensive theoretical modeling study of air-breathing MFCs, based on a semi-empirical Graetz-Domkohler analysis, was also conducted.[88]

Garcia-Cuevas and co-workers[89] numerically analyzed the geometry and operation of MFCs by studying three different fuel cell geometries – the conventional rectangular cell, a cylindrical cell and a star shaped cell – using finite element simulations.

Zhang and co-workers[90] developed a 3D computational model for air-breathing MFCs with flow-over and flow-through anodes. The coupled multiphysics phenomena of fluid flow, species transport and electrochemical reactions were resolved numerically.

Yu and co-workers[91] presented a hierarchical multiscale model for all-vanadium MFCs with porous electrodes, in which the diffusion coefficient is used as a bridge between the microscale, mesoscale and macroscale models. Three-level theories were used to describe the MFC systems, with emphasis on the different time and length scale.

Moein-Jahromi and co-workers[92] performed a comprehensive electrochemical simulation of the cathode catalyst layer using an agglomerate model. With the agglomerate

model, the model can predict cell performance even at high current density when the homogeneous model usually failed.

2.5 Features to be Considered in Model Formulation

Based on the review of modeling for the electrochemical reduction of CO_2 and modeling of MFC discussed in the previous two sections, several conclusions of the features to be considered in model formulation can be drawn:

Basis of Modeling – The models can be classified as physical model and black-box model. Physical model is based on the knowledge of physicochemical characteristics (electrically, chemically and kinematically) while black-box model is empirically determined.[93] Based on the review of models for the electrochemical reduction of CO_2 in other CO_2 electrolyzers and the models of MFCs, in the study of the electrochemical reduction of CO_2 in a microfluidic reactor, physical modeling which presents a higher generalization level that enables modeling cells or stacks of different geometric features will be considered.

Dimensionality – The models discussed in this review range from 0D (simple kinetic model) to 3D, with different features and point to different research objectives. From the point of model functionality, higher dimensional modeling (2D and 3D) is typically concerned with the cell and stack design issues, while lower dimensional modeling (0D and 1D) is aimed at control purposes on the system level. Low dimensional models require less computational time and less information about material properties or electrochemical parameters – whose non-availability might cause troubles in high dimensional models. Higher dimensional models resolve fuller geometry and can provide more information of the performance of the cell. In order to find a balance between model complexity and computational time, top-down approach is adopted by starting with a higher dimensional

model, and subsequently performing reduction in dimensionality, only when it is justified using scaling analysis.

Processes and Governing Equations – The processes to be considered in the mathematical model will include transport in the gas channels, the porous gas diffusion layers and the catalyst layers, material balances in the gas phase in both gas channels and porous gas diffusion layer, electronic and ionic charge balance and charge transfer kinetics. Laws of physics, such as mass and species continuity equations, conservation equations of mass, momentum and charges, together with the electrochemical kinetic equations will be employed in formulating the model.

Parameter Estimation – Parameter estimation of the electrochemical kinetic parameters is unavoidable. The details of the electrochemical reaction mechanisms for this system remain very vague. Accommodating detailed reaction mechanism into the model will entail significant complexity and uncertainty. Simplified kinetic equations with kinetic parameters that are system specific, such as Butler-Volmer kinetic equation, will be employed. Parameter estimation will be performed to calibrate the kinetic parameters.

2.6 Conclusions

This literature review discusses the current development in the electrochemical reduction of CO_2. Due to the lack of existing mathematical model for CO_2 reduction to CO in microfluidic cells, review on the various mathematical models for the electrochemical reduction of CO_2 in other electrolyzers and modeling of MFCs has been conducted. Based on the review, several important features to be considered in our model formulation have been highlighted. A detailed mathematical formulation for the electrochemical reduction of CO_2 in a microfluidic cell will be presented in next chapter.

CHAPTER 3

FULL MATHEMATICAL FORMULATION

3.1 Introduction

In this chapter, the full mathematical model for the electrochemical reduction of CO_2 in a microfluidic cell is introduced. The full cell model starts from the basic physics equations, and integrates the transport of charge, mass and momentum with electrochemistry for both the cathode and anode. A numerical method for solving this model is also proposed. This full mathematical model will be validated in Chapter 4, and be used throughout this thesis to demonstrate various concepts.

3.2 Microfluidic Cells

A CO_2 microfluidic electrolyzer (Figure 3.1) consists of several parallel and rectangular layers and channels of identical lengths and widths and various heights. These include, from top to bottom, a cathode gas channel, a cathode current collector, a cathode gas diffusion electrode (GDE), an aqueous electrolyte channel, an anode GDE, an anode current collector, and an anode gas channel. An aqueous solution enters the electrolyte channel, which is sandwiched between the two GDEs. The GDEs are coated with suitable catalysts on the sides of the electrolyte channel to provide a three-phase interface for electro-chemical reactions. The current collectors on the other side of the GDEs provide electrical contact between the GDEs and an external potentiostat. The feed gas enters the cathode gas channel and exits the CO_2 electrolyzer on the other side along with any cathode-side gaseous products. The anode gas channel is either left open to the atmosphere or can be used to collect the anode-side

gaseous products. In the latter situation, the inlet is closed, and the anode-side gaseous products exit at the other end.

For the conversion of CO_2 to CO studied in this work, the feed gas is a mixture of N_2 and CO_2. The CO_2 in the cathode gas channel diffuses through the top GDE to the cathode catalyst layer (CL). When a neutral or alkaline electrolyte is used, CO_2 is predominantly reduced to CO via reaction (3.1) if a sufficiently high negative cell potential is applied. Water diffuses from the electrolyte to the cathode CL and can be reduced to H_2 via reaction (3.2). The cathode products CO and H_2 together with H_2O vapor diffuse through the top GDE to the cathode gas channel, and exit the cell with unreacted CO_2 and N_2.

$$CO_2 + H_2O + 2e^- \rightarrow CO + 2OH^- \qquad E_{CO} = -0.52 \text{ V (vs SHE)} \qquad (3.1)$$

$$2H_2O + 2e^- \rightarrow H_2 + 2OH^- \qquad E_{H_2} = -0.41 \text{ V (vs SHE)} \qquad (3.2)$$

On the opposite electrode, the oxygen evolution reaction (3.3) takes place in the anode CL, to balance the OH^- produced and the electrons consumed at the cathode. O_2 and H_2O vapor diffuse through the bottom GDE to the anode gas channel and exit the MFC.

$$4OH^- \rightarrow O_2 + 2H_2O + 4e^- \qquad E_{O_2} = +0.82 \text{ V (vs SHE)} \qquad (3.3)$$

3.3 Model Assumptions

The main assumptions underlying our mathematical model are as follows:

(1) The microfluidic cell is at steady state.

(2) The system is isothermal. This is a reasonable assumption due to the presence of a flowing liquid (good thermal conductor) electrolyte, and relatively low current density on the order of 10^2 mA/cm^2 in a microfluidic cell.

(3) Variations along the microfluidic cell width are negligible, so a 2D model is adequate. In practice, the feed gas can be supplied to the cathode gas channel in several ways such as tube, or rectangular channel. the gas feed inlet is assumed to be at the top of the gas channel with a width same as that of the cathode gas channel, but it may have a height less or equal to that of the channel.

(4) The Ohmic loss across a current collector is negligible. The current collectors can thus be treated as interfaces.

(5) The rates of the electrochemical reactions can be described by Butler-Volmer kinetic equation, which is commonly invoked in fuel cell models[83, 84, 94, 95].

(6) Flow in the gas channel is weakly compressible and laminar. Its Reynolds number is on the order of 10^{-2}.

(7) The gas diffusion layers (GDLs) and the CLs of the GDEs are homogeneous porous media, so with isotropic porosity and permeability.

(8) The amount of gaseous species dissolved in the electrolyte is negligible. Negligible effective crossover flux of the gaseous species (CO_2, CO, N_2, H_2 & O_2) was assumed at the electrolyte/CL interface.

(9) The effective conductivity for ionic transport in the electrolyte phase is constant.

3.4 Governing Equations

The simplified schematic of the CO_2 electrolyzer as modeled in this work is shown in Figure 3.1(b). As shown in the figure, the flow direction is taken to be x-direction and the direction along the height of the cell be y-direction. The following processes are taken into

account: multi-component gas transports in the gas channels, porous GDLs and CLs, the material balance in the gas phase (Cathode: CO_2, N_2, CO, H_2 and H_2O; Anode: O_2, H_2O and N_2), the electronic and ionic charge balance, and charge transfer kinetics. This leads to the following governing equations.

Cathode Gas Channel – For a steady 2D flow in the cathode gas channel, the equations for overall mass and momentum balance are:

$$\nabla \cdot (\rho \mathbf{u}) = 0 \tag{3.4}$$

$$\rho \mathbf{u} \cdot \nabla \mathbf{u} = \rho \mathbf{g} - \nabla p + \nabla \cdot \left[\mu (\nabla \mathbf{u} + (\nabla \mathbf{u})^T) - \frac{2}{3} \mu (\nabla \cdot \mathbf{u}) \mathbf{I} \right] \tag{3.5}$$

where ρ is the gas density, $\mathbf{u}$ is the velocity vector, $\mathbf{g}$ is the gravitational acceleration, p is the gas pressure, μ is the dynamic gas viscosity, and $\mathbf{I}$ is the identity tensor. For the species mass balance:

$$\nabla \cdot \mathbf{n}_i \qquad i = \mathrm{CO_2, CO, H_2, H_2O} \tag{3.6}$$

where $\mathbf{n}_i$ is the total mass flux of species (the sum of diffusive and convective mass fluxes) i. To calculate multicomponent flux, Maxwell-Stefan equation is used[96-99]:

$$\mathbf{n}_i = -\rho \omega_i \sum_{j=1}^{N} D_{ij} \left[\frac{M_g}{M_j} \left(\nabla \omega_j + \omega_j \frac{\nabla M_g}{M_g} \right) + (x_j - \omega_j) \frac{\nabla p}{p} \right] + \rho \mathbf{u} \omega_i$$

$$i = \mathrm{CO_2, CO, H_2, H_2O} \tag{3.7}$$

where ω_i is the mass fraction, x_j is the molar fraction, M_g is the molar mass of the gas mixture:

$$M_g = x_{N_2}M_{N_2} + x_{CO_2}M_{CO_2} + x_{CO}M_{CO} + x_{H_2}M_{H_2} + x_{H_2O}M_{H_2O} \tag{3.8}$$

and D_{ij} is the multicomponent diffusion coefficient that can be estimated using the empirical correlation recommended by Fuller, Schettler, and Giddings[100]:

$$D_{ij} = \frac{1.01325 \times 10^{-2} T^{1.75} \left(\frac{1}{M_i} + \frac{1}{M_j}\right)^{1/2}}{p\left(v_i^{1/3} + v_j^{1/3}\right)} \tag{3.9}$$

where T is temperature, p is pressure, and v_i is the diffusion volume for molecule i.

The mass fraction of inert N_2 is then computed from the overall mass balance as,

$$\omega_{N_2} = 1 - \omega_{CO_2} - \omega_{CO} - \omega_{H_2} - \omega_{H_2O} \tag{3.10}$$

Cathode GDL and CL – For the porous medium (GDL and CL), the common equation for the continuity of mass (3.11) and Brinkman's momentum equation (3.12) are used:

$$\nabla \cdot (\rho \mathbf{u}) = Q \tag{3.11}$$

$$\frac{\rho}{\varepsilon}\mathbf{u} \cdot \nabla \frac{\mathbf{u}}{\varepsilon} = \rho \mathbf{g} - \nabla p + \nabla \cdot \left[\frac{\mu}{\varepsilon}\left((\nabla \mathbf{u} + (\nabla \mathbf{u})^T) - \frac{2}{3}(\nabla \cdot \mathbf{u})\mathbf{I}\right)\right] - \left(\frac{\mu}{\kappa}\right)\mathbf{u} \tag{3.12}$$

where Q is the mass source term, which occurs only in the CL where the electrochemical reactions taking place, ε is the average porosity and κ is the average permeability of the

porous medium. The permeability of the GDL can be predicted using the Tomadakis-Sotirchos model[101]:

$$\kappa = \frac{\varepsilon}{8\ln^2 \varepsilon} \frac{\left(\varepsilon - \varepsilon_p\right)^{\alpha+2} {r_f}^2}{\left(1-\varepsilon_p\right)^{\alpha}\left[(\alpha+1)\left(\varepsilon-\varepsilon_p\right)\right]^2} \tag{3.13}$$

where ε_p is the percolation threshold porosity, the porosity with the least required open void space connectivity for diffusion or permeation through the porous media (here $\varepsilon_p = 0.11$), α is a fitting parameter for the through-plan diffusion (here $\alpha = 0.785$), and r_f is the carbon fiber radius (here $r_f = 4.6\ \mu m$).[102]

For species continuity:

$$\nabla \cdot \mathbf{n}_i = R_i \qquad i = \mathrm{CO_2, CO, H_2, H_2O} \tag{3.14}$$

$$\mathbf{n}_i = -\rho\omega_i \sum_{j=1}^{N} D_{ij}^{\mathrm{eff}} \left[\frac{M_g}{M_j}\left(\nabla\omega_j + \omega_j \frac{\nabla M_g}{M_g}\right) + \left(x_j - \omega_j\right)\frac{\nabla p}{p}\right] + \rho\mathbf{u}\omega_i$$

$$i = \mathrm{CO_2, CO, H_2, H_2O} \tag{3.15}$$

where R_i is the reaction rate, which accounts for the consumption of reactants and production of products during the electrochemical reactions in the CL, and D_{ij}^{eff} is the effective gas diffusivity in a porous layer, given by the Bruggeman correction[103] as follows:

$$D_{ij}^{\mathrm{eff}} = \varepsilon^{1.5} D_{ij} \qquad i = \mathrm{CO_2, CO, H_2, H_2O} \tag{3.16}$$

Again, the mass fraction of N_2 is computed from the overall mass balance, Eq. (3.10).

Charge conservation at the cathode GDL is imposed by:

$$\nabla \cdot \mathbf{i} = 0 \tag{3.17}$$

and the current density is given by Ohm's law:

$$\mathbf{i} = -\sigma_{\mathrm{gdl}} \nabla \phi_{\mathrm{s}} \tag{3.18}$$

where σ_{gdl} is the average electronic conductivity of the cathode GDL and ϕ_{s} is the electric potential of the solid phase of the cathode GDE.

In the CL, current can be split into two parts: ionic current and electronic current. Transport of ions in the liquid phase (electrolyte) forms the ionic current, while transport of electrons in the solid phase (electrode) forms the electronic current. The current conservation equations are obtained using Ohm's law:

$$\nabla \cdot \left(-\sigma_{\mathrm{cl\_s}} \nabla \phi_{\mathrm{s}}\right) = S_s \tag{3.19}$$

$$\nabla \cdot \left(-\sigma_{\mathrm{cl\_l}} \nabla \phi_{\mathrm{l}}\right) = S_l \tag{3.20}$$

where $\sigma_{\mathrm{cl\_s}}$ and $\sigma_{\mathrm{cl\_l}}$ are the electronic and ionic conductivity of the CL, ϕ_{s} and ϕ_{l} are the electric potential of the solid phase and liquid phase in the CL, and S_s and S_l are the current source terms resulting from the electrochemical reactions.

Electrolyte channel – For the electrolyte channel, the charge conservation (3.17) holds, and the current follows from Ohm's law as follows:

$$\mathbf{i} = -\sigma_{\text{elec}} \nabla \phi_{\text{l}} \tag{3.21}$$

where σ_{elec} is the average ionic conductivity of the electrolyte and ϕ_{l} is the electric potential of the liquid electrolyte.

Anode CL and GDL – If the anode gas channel is open to the atmosphere, convection in the CL and GDL is negligible compared to diffusion. For species continuity:

$$\nabla \cdot \mathbf{n}_i = R_i \qquad i = \text{O}_2, \text{H}_2\text{O} \tag{3.22}$$

$$\mathbf{n}_i = -\rho \omega_i \sum_{j=1}^{N} D_{ij} \left[\frac{M_g}{M_j} \left(\nabla \omega_j + \omega_j \frac{\nabla M_g}{M_g} \right) + \left(x_j - \omega_j \right) \frac{\nabla p}{p} \right] \qquad i = \text{O}_2, \text{H}_2\text{O} \tag{3.23}$$

Again, the effective diffusivity in the porous layer is modified using the Bruggeman correction. The mass fraction of N_2 is given by

$$\omega_{\text{N}_2} = 1 - \omega_{\text{O}_2} - \omega_{\text{H}_2\text{O}} \tag{3.24}$$

If the O_2 produced at the anode is to be collected, the anode compartment will only have one outlet, so in steady state only O_2 and H_2O vapor will be present in the anode gas channel and anode GDE. In this case, Eqs. (3.11) – (3.16) can be used to describe the continuity of mass and momentum, and transport of species (O_2 and H_2O) in the porous anode GDL and CL.

The current densities in the anode GDL and CL can be described using Eqs. (3.17) – (3.20).

Anode Gas Channel – If the anode gas channel is open to the atmosphere, then Eqs. (3.22) – (3.24) can be used for the anode gas channel as well, but with D_{ij} in place of D_{ij}^{eff}. If the compartment is not open to the atmosphere, except for one outlet for the formed O_2 to escape, then Eqs.(3.4) – (3.7) are used for O_2 and H_2O vapor.

3.5 Electrochemical Reaction Kinetics

In contrast to formate formation in aqueous media, the proposed reaction scheme for CO formation from CO_2 electro-reduction is heterogeneous, involving the adsorption of radicals and further reaction on the metal-catalytic surface.[58] Instead of considering dissolved CO_2, direct adsorption of gaseous CO_2 onto the catalyst surface is assumed. For simplicity, only the gas phase species transport in the CL is accounted for, concentration of CO_2 gas instead of dissolved CO_2 was used in the rate equation.

The details of the electrochemical catalytic reaction mechanisms are still very vague. Accommodating detailed reaction mechanisms into the model will entail significant complexity and uncertainty. The rates of the electrochemical reactions are assumed to follow Butler-Volmer kinetics equation, which is commonly invoked in fuel cell models[83, 84, 90, 94, 95].

Cathode CL – The rate of formation of CO in the cathode CL depends on the local concentration of CO_2 at the active sites in the CL. As the CL is adjacent to the flowing aqueous electrolyte, it is reasonable to assume the active sites saturated with water and no dependence of water concentration in the rate expression. Thus, the transfer current density corresponding to the formation of CO is given by:

$$i_{\mathrm{CO}} = i_{\mathrm{CO,ref}} \frac{C_{\mathrm{CO_2}}}{C_{\mathrm{CO_2,ref}}} \exp\left(-\frac{\alpha_{\mathrm{CO}} F}{RT} \eta_{\mathrm{CO}}\right) \tag{3.25}$$

where $i_{\mathrm{CO,ref}}$ is the exchange current density, $C_{\mathrm{CO_2}}$ is the local CO_2 concentration, $C_{\mathrm{CO_2,ref}}$ is the reference CO_2 concentration, α_{CO} is the charge transfer coefficient, F is the Faraday constant, R is the universal gas constant, T is the system temperature, and η_{CO} is the overpotential of the CO formation reaction at the cathode. The CO overpotential is given by:

$$\eta_{\mathrm{CO}} = \phi_{\mathrm{s}} - \phi_{\mathrm{l}} - E_{\mathrm{CO}} \tag{3.26}$$

where E_{CO} is the reversible potential of the half reaction for CO formation, ϕ_{s} and ϕ_{l} are the local electric and electrolyte potential derived from Eq. (3.19) and Eq. (3.20).

The experiments by Whipple[104] revealed that cell performance is independent of the electrolyte pH for the electrochemical reduction of CO_2 to CO in a microfluidic cell using an aqueous flowing electrolyte. Thus, the kinetics of the electrochemical reactions can be treated as being independent of the concentrations of H^+ and OH^- ions under the range of operating conditions studied. The transfer current density corresponding to the formation of H_2 at the cathode then can be expressed as:

$$i_{\mathrm{H_2}} = i_{\mathrm{H_2,ref}} \exp\left(-\frac{\alpha_{\mathrm{H_2}} F}{RT} \eta_{\mathrm{H_2}}\right) \tag{3.27}$$

where $i_{\mathrm{H_2,\,ref}}$ is the exchange current density and $\alpha_{\mathrm{H_2}}$ is the charge transfer coefficient for this reaction. The overpotential $\eta_{\mathrm{H_2}}$ is given by:

$$\eta_{H_2} = \phi_s - \phi_l - E_{H_2} \tag{3.28}$$

where E_{H_2} is the reversible potential of the half reaction for H_2 formation.

The reaction rates R_i at the cathode CL in Eq. (3.14) are then given by:

$$\begin{aligned} R_{CO_2} &= -\frac{a_{CO} i_{CO}}{2F} M_{CO_2} \\ R_{H_2O} &= -\frac{a_{CO} i_{CO}}{2F} M_{H_2O} - \frac{a_{H_2} i_{H_2}}{F} M_{H_2O} \\ R_{CO} &= \frac{a_{CO} i_{CO}}{2F} M_{CO} \\ R_{H_2} &= \frac{a_{H_2} i_{H_2}}{2F} M_{H_2} \end{aligned} \tag{3.29}$$

where a_{CO} and a_{H_2} are the specific surface (ratio of reaction surface of the active sites to catalyst layer volume).

The mass source term Q in Eq. (3.11) is then given by:

$$Q = R_{CO_2} + R_{CO} + R_{H_2} + R_{H_2O} \tag{3.30}$$

The current source terms S_s and S_l in Eq. (3.19) and Eq. (3.20) are given by:

$$S_s = -\left(a_{CO} i_{CO} + a_{H_2} i_{H_2}\right), \quad S_l = a_{CO} i_{CO} + a_{H_2} i_{H_2} \tag{3.31}$$

Anode CL – At the anode CL, only O_2 formation reaction takes place. The transfer current density for O_2 formation reaction can be described by:

$$i_{O_2} = i_{O_2,\text{ref}} \exp\left(\frac{\alpha_{O_2} F}{RT} \eta_{O_2}\right) \tag{3.32}$$

where $i_{O_2,\text{ ref}}$ is the exchange current density and α_{O_2} is the charge transfer coefficient for this reaction. The overpotential η_{O_2} is given by:

$$\eta_{O_2} = \phi_s - \phi_l - E_{O_2} \tag{3.33}$$

where E_{O_2} is the reversible potential of the half reaction for O_2 formation.

The reaction rates R_i at the anode CL in Eq. (3.22) are then given by:

$$R_{O_2} = \frac{a_{O_2} i_{O_2}}{4F} M_{O_2}, \qquad R_{H_2O} = \frac{a_{O_2} i_{O_2}}{2F} M_{H_2O} \tag{3.34}$$

The mass source term Q in Eq. (3.11) is then given by:

$$Q = R_{O_2} + R_{H_2O} \tag{3.35}$$

The current source terms S_s and S_l in Eqs. (3.19) and (3.20) are given by:

$$S_s = a_{O_2} i_{O_2}, \quad S_l = -a_{O_2} i_{O_2} \tag{3.36}$$

The overall applied cell potential is defined as:

$$V_{\text{cell}} = V_{\text{cath}} - V_{\text{anod}} \tag{3.37}$$

where V_{cath} and V_{anod} are the electric potentials applied at the cathode and anode current collectors respectively.

3.6 Boundary Conditions

Cathode Gas Channel – At the cathode gas inlet (I), composition and flow rate are constant:

$$\mathbf{u} \cdot \mathbf{e}_{\boldsymbol{x}} = U_{\text{g,in}}$$
$$\omega_{\text{CO}_2} = \omega_{\text{CO}_2,\text{in}}, \qquad \omega_{\text{CO}} = 0, \qquad \omega_{\text{H}_2} = 0, \qquad \omega_{\text{H}_2\text{O}} = 0 \tag{3.38}$$

where $\mathbf{e}_{\boldsymbol{x}}$ is the unit vector in the x-direction, i.e. along the flow direction, $U_{\text{g, in}}$ is the average normal inflow velocity, and $\omega_{\text{CO}_2,\text{in}}$ is the mass fraction of CO_2 in the feed gas.

At the cathode gas outlet boundary (II), a constant reference pressure p_{exit} and fully developed flow with no viscous stress and no diffusive species fluxes are assumed:

$$p = p_{\text{exit}}$$
$$\left(\mu(\nabla\mathbf{u} + (\nabla\mathbf{u})^T) - \frac{2}{3}\mu(\nabla \cdot \mathbf{u})\mathbf{I}\right)\mathbf{e}_{\boldsymbol{x}} = \mathbf{0} \tag{3.39}$$
$$\mathbf{n_i} \cdot \mathbf{e}_{\boldsymbol{x}} = 0 \qquad i = \text{CO}_2, \text{CO}, \text{H}_2, \text{H}_2\text{O}$$

At the outer walls of the cathode gas channel (III & IV), the no-slip condition is assumed applicable and the walls are impermeable:

$$\mathbf{u} \cdot \mathbf{e}_{\boldsymbol{x}}|_{\text{III}} = 0, \qquad \mathbf{n_i} \cdot \mathbf{e}_{\boldsymbol{x}}|_{\text{III}} = 0 \qquad i = \text{CO}_2, \text{CO}, \text{H}_2, \text{H}_2\text{O} \tag{3.40}$$

$$\mathbf{u} \cdot \mathbf{e}_{\boldsymbol{x}}|_{\mathrm{IV}} = 0, \qquad \mathbf{n}_{\mathbf{i}} \cdot \mathbf{e}_{\boldsymbol{x}}|_{\mathrm{IV}} = 0 \qquad i = \mathrm{CO_2, CO, H_2, H_2O} \quad (3.41)$$

Cathode Gas-Channel-GDL Interface – The electric potential at this interface is the applied cathode potential V_{cath}:

$$\phi_{\mathrm{s}} = V_{\mathrm{cath}} \quad (3.42)$$

Cathode GDL and CL – At the vertical walls of the porous GDL and CL (VI), symmetrical conditions for slip walls (no normal flow and no species fluxes) and charge insulation are specified,

$$\mathbf{u} \cdot \mathbf{e}_{\boldsymbol{x}} = 0, \ \mathbf{n}_{\mathbf{i}} \cdot \mathbf{e}_{\boldsymbol{x}} = 0 \, , \ \mathbf{i} \cdot \mathbf{e}_{\boldsymbol{x}} = 0 \qquad i = \mathrm{CO_2, CO, H_2, H_2O} \quad (3.43)$$

Cathode CL-Electrolyte Interface – No normal flow and no crossover fluxes at this interface (VII) are assumed:

$$\mathbf{u} \cdot \mathbf{e}_{\boldsymbol{y}} = 0, \ \mathbf{n}_{\mathbf{i}} \cdot \mathbf{e}_{\boldsymbol{y}} = 0 \qquad i = \mathrm{CO_2, CO, H_2, H_2O} \quad (3.44)$$

Water in the electrolyte is in equilibrium with H_2O vapor in the gas phase. The mass fraction of H_2O vapor at this interface can be calculated from its vapor pressure p_{sat}:

$$\omega_{\mathrm{H_2O}} = \frac{p_{sat} M_{\mathrm{H_2O}}}{p M_g} \quad (3.45)$$

where M_g is the molar mass of the gas mixture.

Anode CL-Electrolyte Interface – No normal flow, no crossover fluxes and saturated H-$_2$O vapor at this interface (VIII) are assumed:

$$\mathbf{u} \cdot \mathbf{e}_{\boldsymbol{y}} = 0, \qquad \mathbf{n}_{\mathrm{O_2}} \cdot \mathbf{e}_{\boldsymbol{y}} = 0, \qquad \omega_{\mathrm{H_2O}} = \frac{p_{sat} M_{\mathrm{H_2O}}}{p M_g} \tag{3.46}$$

Anode GDL and CL – At the vertical walls of the porous GDL and CL (IX), symmetrical conditions for slip walls (no normal flow and no species fluxes) and charge insulation are specified,

$$\mathbf{u} \cdot \mathbf{e}_{\boldsymbol{x}} = 0, \qquad \mathbf{n}_{\mathbf{i}} \cdot \mathbf{e}_{\boldsymbol{x}} = 0\,, \qquad \mathbf{i} \cdot \mathbf{e}_{\boldsymbol{x}} = 0 \qquad i = \mathrm{O_2},\ \mathrm{H_2O} \tag{3.47}$$

Anode Gas-Channel-GDL Interface – The electric potential at this interface equals the applied anode potential V_{anod}:

$$\phi_{\mathrm{s}} = V_{\mathrm{anod}} \tag{3.48}$$

Anode Gas Channel – If the anode is open to the atmosphere, then both inlet and outlet of the gas channel are closed and the wall (XIII) is open. At the vertical walls (XI and XII), no diffusive fluxes are specified:

$$\mathbf{n}_{\mathbf{i}} \cdot \mathbf{e}_{\boldsymbol{x}}|_{\mathrm{XI}} = 0,\ \mathbf{n}_{\mathbf{i}} \cdot \mathbf{e}_{\boldsymbol{x}}|_{\mathrm{XII}} = 0 \qquad i = \mathrm{O_2},\ \mathrm{H_2O} \tag{3.49}$$

and at the opening (XIII), a constant mass fraction of O_2 can be specified as it is exposed to the atmosphere which can be considered as a bulk phase of constant composition:

$$\omega_{O_2} = \omega_{O_2,\text{ref}} \tag{3.50}$$

If the O_2 produced is to be collected, then the inlet (XI) is still closed, but the outlet (XII) is open. No-slip condition is applied to the inlet (XI) and the horizontal wall (XIII):

$$\mathbf{u} \cdot \mathbf{e}_{\boldsymbol{x}}|_{\text{XI}} = 0 \tag{3.51}$$

$$\mathbf{u} \cdot \mathbf{e}_{\boldsymbol{y}}\big|_{\text{XIII}} = 0 \tag{3.52}$$

At the outlet, a reference pressure is specified and no viscous stress is assumed:

$$p = p_{\text{exit}}, \qquad \left(\mu(\nabla\mathbf{u} + (\nabla\mathbf{u})^T) - \frac{2}{3}\mu(\nabla \cdot \mathbf{u})\mathbf{I}\right)\mathbf{e}_{\boldsymbol{x}} = \mathbf{0} \tag{3.53}$$

3.7 Cell Performance Measures

Current Densities – Current density reflects the rate of an electrochemical reaction. The computed average partial current density is the integrated average of the local current densities at the cathode CL for a given species:

$$i_{\text{CO}}^{\text{num}} = \frac{1}{L}\int_0^{H_{cl}}\int_0^{L} a_{\text{CO}} i_{\text{CO}}\, dxdy \tag{3.54}$$

$$i_{\text{H}_2}^{\text{num}} = \frac{1}{L}\int_0^{H_{cl}}\int_0^{L} a_{\text{H}_2} i_{\text{H}_2}\, dxdy \tag{3.55}$$

Specifically, the average partial current density $i_{\text{CO}}^{\text{num}}$ reflects CO_2 conversion rate.

Then, the computed average total current density is:

$$i_{\text{total}}^{\text{num}} = i_{\text{CO}}^{\text{num}} + i_{\text{H}_2}^{\text{num}} \tag{3.56}$$

Faradaic Efficiency – This reflects the selectivity of the primary reaction (here CO formation). It is computed using the following equation:

$$\text{FE}\ (\%) = \frac{i_{\text{CO}}^{\text{num}}}{i_{\text{total}}^{\text{num}}} \times 100\% \tag{3.57}$$

Conversion per pass – The conversion of CO_2 per pass is specified by:

$$\text{Conv}\ (\%) = \frac{\int_0^{H_{\text{gtop}}} \mathbf{n}_{\text{CO}_2} \cdot \mathbf{e}_{\boldsymbol{x}}\big|_{\text{I}}\, dy - \int_0^{H_{\text{gtop}}} \mathbf{n}_{\text{CO}_2} \cdot \mathbf{e}_{\boldsymbol{x}}\big|_{\text{II}}\, dy}{\int_0^{H_{\text{gtop}}} \mathbf{n}_{\text{CO}_2} \cdot \mathbf{e}_{\boldsymbol{x}}\big|_{\text{I}}\, dy} \times 100\% \tag{3.58}$$

3.8 Numerical Method

The full set of governing equations together with boundary conditions, electrochemical reaction kinetic equations and other constitutive equations, Eqs. (3.4) – (3.58) in previous sections, were solved numerically with COMSOL Multiphysics[105]. COMSOL Multiphysics is a software for the solution of systems of partial differential equations (PDEs) based on finite element method for the spatial discretization. The model was implemented in COMSOL 4.3b using the base case parameters in Table 3.1, and solved using the direct solver, PARDISO, with a relative convergence tolerance of 10^{-6}, through a fully coupled approach. A coarse mesh of about 2500 elements for the unit cell in Figure 3.1(b) was first used. Consecutive mesh adaptation of up to 120000 elements allowed for high resolution in the GDEs. Mesh independence was ensured by ensuring that successive mesh adaptations did

not change CO_2 conversion by more than 0.1%. One simulation takes 3-8 minutes on an Intel® Core™ i7-3770 CPU @ 3.40 GHz PC with 16.0 GB RAM.

3.9 Conclusions

In this chapter, a steady state and isothermal 2D electrochemical model for CO_2 reduction to CO in a microfluidic flow cell is presented. The model accounts for all the significant physics and electrochemistry in the cell, including the transport of species and charges, momentum and mass conservation, and electrochemical reactions. Due to incomplete knowledge of the underlying electrochemical catalytic reactions and excessive complexity of accommodating reaction mechanisms into the fluidic flow model, electrochemical kinetic parameters, in this case the charge transfer coefficients and the exchange current densities need to be calibrated based on experimental results. Results of parameter estimation will be presented in Chapter 4. The calibrated model will also be experimentally validated, to ensure the credibility of model prediction. The validated model will then be used for parametric study in Chapter 5. It will also serve as the base model for deriving the reduced model in Chapter 6.

3.10 Figure

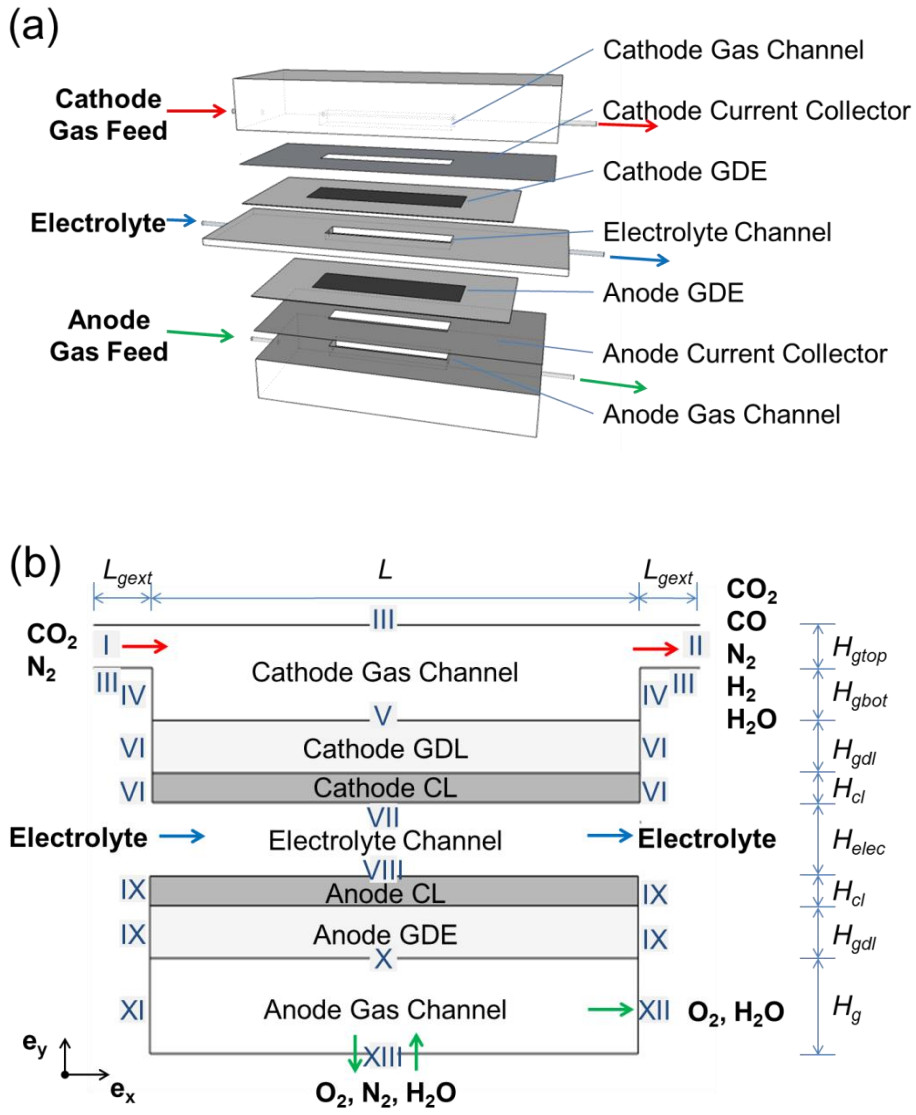

Figure 3.1. (a) A schematic of the various functional layers in a microfluidic cell for CO_2 reduction and (b) Simplified schematic used in modeling. Boundaries are marked with Roman numerals: (I) cathode gas channel inlet; (II) cathode gas channel outlet; (III) cathode gas channel horizontal walls; (IV) cathode gas channel vertical walls; (V) cathode gas-channel-GDL interface; (VI) cathode GDE vertical walls; (VII) cathode CL-electrolyte interface; (VIII) anode CL-electrolyte interface; (IX) anode GDE vertical walls; (X) anode gas-channel-GDL interface; (XI) anode gas channel wall/inlet; (XII) anode gas channel wall/outlet; (VIII) anode gas channel wall/opening.

3.11 Table

Table 3.1. Key parameter values used in simulation

Parameter	**Symbol**	**Base Case / (Range)**	**Unit**	**Source**
	Operating Condition			
Temperature	T	298	K	measured
Exit pressure	P_{exit}	1.0	atm (abs)	measured
Feed gas flow rate	Q_g	7 (2 – 42)	sccm	measured
Feed CO_2 molar fraction	$x_{CO_2,in}$	0.2 (0.05 – 0.35)	-	measured
Applied cell potential	V_{cell}	−3.0 (−2.2 – −3.2)	V	measured
pH	pH	7.0	-	measured
	Microfluidic Cell Geometry			
Channel length	L	0.02 (0.01 – 0.4)	m	measured
Extended length of the gas channel	L_{gext}	0.002	m	measured
Width of the channel	W	0.005	m	measured
Height of the upper portion of the gas channel	H_{gtop}	5.08×10^{-4}	m	measured
Height of the lower portion of the gas channel	H_{gbot}	1.49×10^{-3}	m	measured
Height of the GDL	H_{gdl}	3.00×10^{-4}	m	measured
Height of the CL	H_{cl}	8×10^{-6}	m	[102]
Height of the electrolyte channel	H_{elec}	1.50×10^{-3}	m	measured
	Fluidic Properties			
Dynamic viscosity of gas (estimated using N_2)	μ	1.7855×10^{-5}	Pa·s	[106]
Ionic conductivity of the electrolyte	σ_{elec}	15.0	S/m	calculated for 1M of KCl [107]
Water vapor pressure	p_{sat}	3187.7	Pa (abs)	[108]
Diffusion volume for CO_2	v_{CO_2}	26.9	-	[100, 106]
Diffusion volume for CO	v_{CO}	18.9	-	[100, 106]
Diffusion volume for H_2	v_{H_2}	6.12	-	[100, 106]
Diffusion volume for N_2	v_{N_2}	17.9	-	[100, 106]
Diffusion volume for O_2	v_{O_2}	16.6	-	[100, 106]
Diffusion volume for H_2O	v_{H_2O}	12.7	-	[100, 106]
	Electrode Properties			
Porosity of GDL	ε	0.663 (0.4 – 0.8)	-	[102]
Porosity of CL	ε_{cl}	0.4	-	[90]
Electronic conductivity of the GDL	σ_s	50000	S/m	[102]
Electronic conductivity of the solid phase of CL	σ_{cl_s}	0.727×10^5	S/m	[90]
Ionic conductivity of the liquid phase of CL	σ_{cl_l}	0.0657	S/m	[90]

CHAPTER 4

PARAMETER ESTIMATION AND MODEL VALIDATION

4.1 Introduction

In Chapter 3, a full mathematical model comprised of conservation laws of physics and electrochemical kinetic equations was developed for the electrochemical reduction of CO_2 in a microfluidic cell. The kinetic parameters (e.g. transfer coefficients and exchange current densities) in the model formulation are system specific and must be calibrated with the help of experimental data. With the estimated kinetic parameters, the model will be further validated using an independent set of experimental data, so as to ensure that the model is indeed predicting the performance of an actual microfluidic cell. These parameter estimation and model validation steps are very crucial as they establish the credibility of the model predictions against an actual cell. In this chapter, the results of parameter estimation and model validation will be presented.

4.2 Experiments[1]

The reactor design and experimental setup were similar to the experimental study by Whipple et al.[19]. The electrolyte channel was prepared by machining a 0.5 cm wide by 2.0 cm long channel in a 1.5 mm thick polyether ether ketone (PEEK) window. The GDEs were prepared by applying catalyst ink via hand-painting on Sigracet 35BC gas diffusion layers (GDLs, Ion Power). Catalyst loading was 0.9 mg Ag/cm^2 and 1.0 mg Pt/cm^2 for the cathode and anode respectively. The cathode gas channel was a 0.5 cm wide by 2.0 cm long by 2 mm deep window in an aluminium block. The anode was left open to the atmosphere. The

[1] This experimental work is the contribution of Mr. Byoungsu Kim from The Kenis Research Group in the University of Illinois at Urbana-Champaign.

assembly was held together with four bolts with Teflon washers to maintain electric isolation between electrodes. The dimensions and material properties of the microfluidic cell are summarized in Table 3.1 as base case values.

The experiments were conducted at room temperature (298 K) with the outlet streams exposed to ambient pressure (1.0 atm). An aqueous stream of 1 M KCl at a flow rate of 0.4 ml/min was used as the electrolyte. The experiments were performed at six feed gas flows as summarized in Table 4.1. For each flow, the cell potential was varied from –2.25 V to –3.00 V at –0.25 V intervals. Thus, 24 independent data sets were obtained. Cell polarization curves were recorded by steady-state chrono-amperometric measurements. Individual anode and cathode polarization curves were measured using an Ag/AgCl reference electrode (RE-5B, BASi) that was placed in the outlet reservoir of the electrolyte.

4.3 Fitting Measures

Out of the 24 sets of experimental data, 16 sets were used in parameter estimation while the remaining 8 sets were used in model validation. To obtain the best fits for the six kinetic parameters (α_{CO}, α_{H_2}, α_{O_2}, $a_{CO} i_{CO,ref}$, $a_{H_2} i_{H_2,ref}$ and $a_{O_2} i_{O_2,ref}$), the discrepancy between the simulated and experimental results needs to be minimized. To this end, root mean squared error (RMSE) between the experimental and simulated (numerical) average current densities is defined as the objective function:

$$\text{RMSE} = \sqrt{\frac{1}{16}\sum_{k=1}^{16}\left(i_{\text{total}}^{\text{num}} - i_{\text{total}}^{\text{exp}}\right)^2} \tag{4.1}$$

where k is the index for the 16 experimental runs used for parameter estimation.

Another measure for the quality of the fit is the percent error in the individual current density, which quantifies the error associated with each simulated average current density when the experimental data is available and is non-zero:

$$\mathrm{err}_i(\%) = \frac{i_i^{\mathrm{num}} - i_i^{\mathrm{exp}}}{i_i^{\mathrm{exp}}} \times 100\% \tag{4.2}$$

4.4 Results and Discussions

The COMSOL model formulated as discussed in Chapter 3 was exported into MATLAB 2012b[109] and used a coordinate search global optimization algorithm (DIRECT[110]) to minimize the function in Eq. (4.1). The best-fit parameter values obtained are shown in Table 4.2.

Figure 4.1 compares the experimentally measured polarization curves with the model predictions. Good agreement is observed with a RMSE of 1.34 mA/cm^2 during estimating the electrochemical reaction kinetic parameters and RMSE of 2.22 mA/cm^2 during model validation. The fit at the high cell potentials of around –3.0 V is very good, with an average percent error of 3.3% during parameter estimation and 4.5% during model validation. This is desirable, as the cell will usually operate at potentials negative than –2.5 V.

4.5 Verification of 2D Assumption

In Chapter 3, it was assumed during model formulation that 2D model is adequate. To verify this assumption further, the model is extended to a 3D model. Same governing equations and boundary conditions as discussed for the 2D model are applied to the 3D model. As for the additional outer walls of the gas channel, similar to interface (III) and (IV), no-slip condition and impermeable wall conditions, i.e. Eq. (3.40) and (3.41), are applied. As

for the additional outer walls of the GDL and CL, similar to interface (VI), symmetrical conditions for slip walls (no normal flow and no species fluxes) and charge insulation, i.e. Eq. (3.43), are applied. Using the same calibrated kinetic parameters as reported in Table 4.2, simulations using the 3D model were performed, with feed flow rate and composition as specified in Table 4.1 and other operating conditions taking the base case values in Table 3.1.

Figure 4.2 shows the comparison of polarization curves obtained via 2D and 3D simulations. The RMSE in the 3D polarization curve as compared to the 2D simulation results is only 0.32 mA/cm^2, while the average difference between the two curves is less than 3%. Good agreement is observed between the 3D and 2D simulation results. The 2D assumption is justified. In terms of computational time, one run of simulation using the 3D model takes more than 1 hour while that using the 2D model only takes 3-8 minutes on an Intel® Core™ i7-3770 CPU @ 3.40 GHz PC with 16.0 GB RAM. In view of the negligible difference in simulation results and significant increase in computational time while using the 3D model, 2D model is sufficient for this system.

4.6 Conclusions

In this chapter, the values of the kinetic parameters in the electrochemical reaction rate equations as formulated in the previous chapter have been determined using a set of experimental data. The parameterized model has been subsequently validated by comparing simulation results with an independent set of experimental data. The simulation results successfully predict a set of polarization curves obtained at different feed gas flow rate and gas feed compositions. Use of this validated model to study the characteristics of the cell will be demonstrated in the next chapter.

4.7 Figures

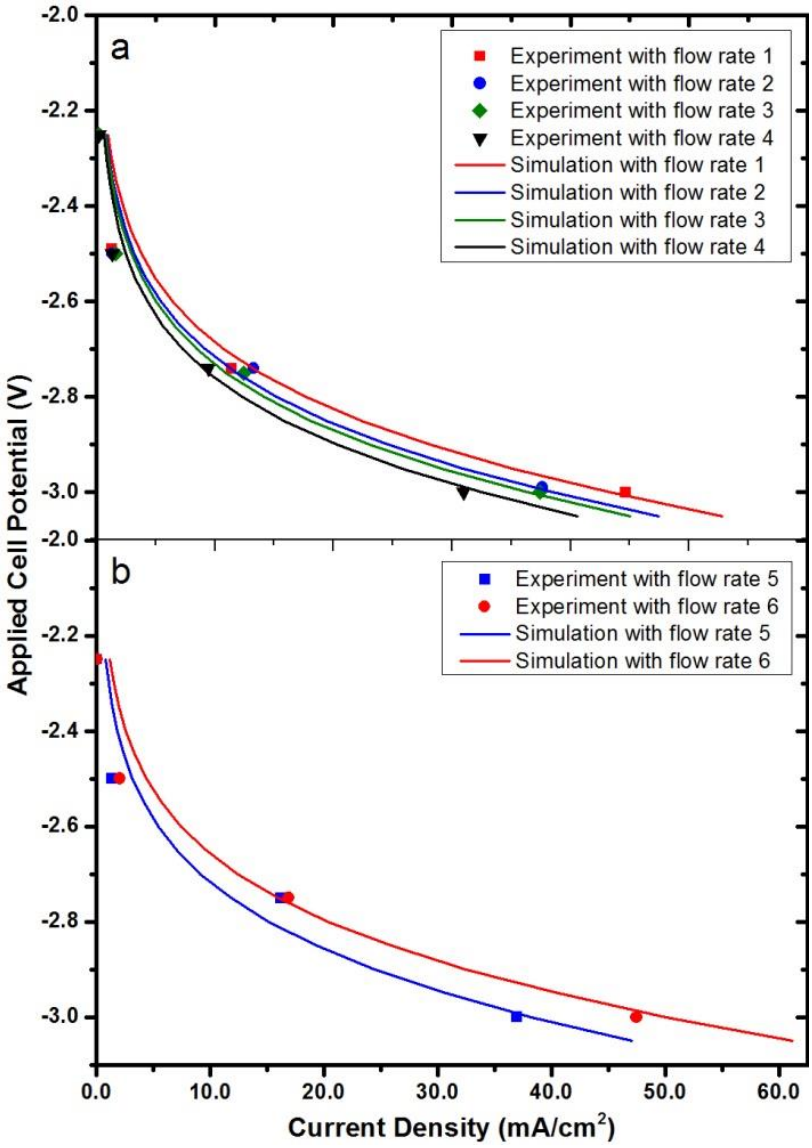

Figure 4.1. Comparison of polarization curves for (a) parameter estimation and (b) model validation. Feed gas flow rate and compositions are specified in Table 4.1. Other operating conditions take the base case values in Table 3.1.

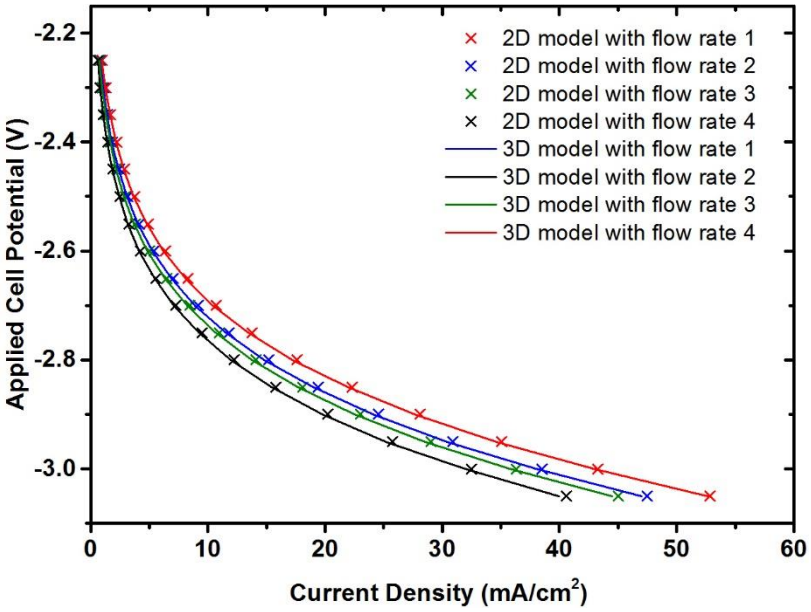

Figure 4.2. Comparison of polarization curves obtained via 2D and 3D simulations. Feed gas flow rate and compositions are specified in Table 4.1. Other operating conditions take the base case values in Table 3.1.

4.8 Tables

Table 4.1. Experimental setting for feed gas flow rate and compositions

Experiment No.	**Parameter Estimation**				**Validation**	
	1	**2**	**3**	**4**	**5**	**6**
Feed CO_2 flow rate (sccm)	1.5	1.5	1.5	1.5	1.4	3.0
Feed N_2 flow rate (sccm)	4.6	6.1	7	9	5.6	7.0

Table 4.2. Parameters in the electrochemical reaction kinetic equations

Parameter	Symbol	Value	Unit
Reversible potential of CO formation half-cell	E_{CO}	–0.52	V (at pH 7 vs SHE)
Reversible potential of H_2 formation half-cell	E_{H2}	–0.41	V (at pH 7 vs SHE)
Reversible potential of O_2 formation half-cell	E_{O2}	0.82	V (at pH 7 vs SHE)
Reference CO_2 concentration	$C_{\mathrm{CO_2,ref}}$	40.9	mol/m^3
Exchange current density × specific surface, CO formation	$a_{\mathrm{CO}} i_{\mathrm{CO,\ ref}}$	1.28×10^5	A/m^3
Exchange current density × specific surface, H_2 formation	$a_{\mathrm{H_2}} i_{\mathrm{H_2,\ ref}}$	48.3	A/m^3
Exchange current density × specific surface, O_2 formation	$a_{\mathrm{O_2}} i_{\mathrm{O_2,\ ref}}$	9.98×10^{-2}	A/m^3
Charge transfer coefficient of CO formation half-cell	α_{CO}	0.17	-
Charge transfer coefficient of H_2 formation half-cell	$\alpha_{\mathrm{H_2}}$	0.25	-
Charge transfer coefficient of O_2 formation half-cell	$\alpha_{\mathrm{O_2}}$	0.79	-

CHAPTER 5

PARAMETRIC STUDIES

5.1 Introduction

A full mathematical model for the electrochemical reduction of CO_2 in a microfluidic cell was presented in Chapter 3. This model was parameterized and validated in Chapter 4. In this chapter, the validated parameterized model will be used to analyze the electrochemical characteristics of the cell, and the effects of several operating parameters and design parameters on the performance of the cell.

5.2 Electrochemical Characteristics

To analyze the electrochemical characteristics of the cell, the effect of applied cell potential on the current densities was investigated. Figure 5.1 presents the simulated current-potential profiles. As the applied cell potential increases (becomes more negative), the current densities for both CO and H_2 formations increase. The undesirable side reaction of H_2 formation accounts for less than 10% of the total current density for applied cell potentials below –2.8 V. A more negative cell potential is required for the onset of H_2 formation compared to CO formation. As predicted by the larger charge transfer coefficient, H_2 production increases much faster than CO formation at high cell potentials, leading to a decrease in the Faradaic efficiency. Thus, if CO is the only desired product, an intermediate optimal potential exists. In contrast, for syngas production, a suitable potential should be chosen to obtain the desired CO to H_2 ratio.

5.3 Studies of Operating Parameters

Operating parameters such as feed CO_2 composition and feed gas flow rate affects the performance of the cell significantly.

Effects of Feed CO_2 Composition – The CO_2 fraction in flue gas varies. Simulations with different feed CO_2 composition were performed. Figure 5.2 shows the effects of CO_2 concentration on cell performance for fixed feed gas flow rates. The average partial current density for CO formation demonstrates a nearly linear increase from 2.5 to 50 mA/cm^2 as CO_2 concentration of the feed increases from 1 to 35 vol%. The Faradaic efficiency increases from 22% to 77%, while the CO_2 conversion decreases from 30% to 24%, for an initial increase from 1 vol% to 10 vol% in the CO_2 concentration of the feed. However, upon a further increase in CO_2 concentration, the rate of increase in Faradaic efficiency and the rate of decrease in CO_2 conversion drop. As the CO_2 concentration in the feed increases, its concentration at the active sites in the CL also increases, leading to an increase in current density and Faradaic efficiency. This confirms that the kinetics of CO_2 reduction depends significantly on the CO_2 concentration at the active sites. Therefore, modifying the GDEs such that they enhance CO_2 transport to the CL is critical for improving cell performance.

Effects of Feed Gas Flow Rate – The effects of the feed gas flow rate at constant CO_2 concentrations on cell performance are shown in Figure 5.3. As the feed gas flow rate increases from 1 to 6 sccm, the average CO partial current density increases by more than 50% and the Faradaic efficiency increases from 78% to 88%. At higher feed rate, the average CO_2 concentration in the flow channel is higher and thus a higher CO_2 concentration is present in the CL. Therefore, higher feed gas flow increases the rate of reaction and thus current density. However, when the CO_2 concentration in the CL exceeds a certain limit, the effect of overpotential dominates over mass transport. Any further increase in that

concentration has a negligible effect on the reaction kinetics. This is confirmed by the fact that the CO partial current density and Faradaic efficiency level off when the feed rate exceeds 15 sccm. A higher feed rate also implies a shorter residence time. The decrease in residence time cannot be compensated by the increase in reaction kinetics, resulting in a decrease in CO_2 conversion, as shown in Figure 5.3. Operating the reactor at higher feed rate and thus higher throughput is desirable, as it lowers both the operating cost (high Faradaic efficiency) and capital cost (higher CO_2 conversion rate (mol/m^2-s)).

5.4 Studies of Design Parameters

This section demonstrates the use of the model for analyzing the effects of design parameters such as channel length and electrode porosity.

Effects of Channel Length – From a design perspective, analyzing the effect of channel length on cell performance is useful. As demonstrated in Figure 5.4, upon increasing the channel length from 0.01 to 0.35 m, the CO_2 conversion increases from 13% to 99%, but the average partial current density corresponding to CO formation drops from 35 to 10 mA/cm^2 and the Faradaic efficiency decreases almost linearly from 89% to 57%. The former can be explained by the fact that a longer channel leads to a larger active surface for electrochemical reaction, thus improving CO_2 conversion. However, longer channel leads to lower average CO_2 concentration in the cell because of depletion of the reactant CO_2 and dilution effect of the product gaseous CO and H_2, resulting in smaller average current density. The side reaction (H_2 evolution) is independent of the composition of the gas in the channel, so the electrical energy consumption associated with the side reaction increases with channel length, resulting in a decrease in the Faradaic efficiency. During design, this model can be employed to determine the minimum channel length for a given CO_2 conversion.

Effects of Electrode Porosity – The effect of increasing the porosity of GDL on cell performance is shown in Figure 5.5. Increased porosity indeed leads to a higher Faradaic efficiency, CO_2 conversion and CO partial current density. However, the improvements are less than 1% for all the three performance measures for a porosity change from 0.40 to 0.75. This suggests that considering porosity of the GDL is not needed in optimizing cells for better performance.

5.5 Conclusions

In this chapter, the results of parametric studies are presented. The parametric studies performed allow us to obtain a general idea of the behavior of the CO_2 electrochemical reduction in a microfluidic flow cell when some cell parameters are changes. The simulation results reveal the importance of improving CO_2 transport in the GDEs, as well as the limited effects on cell performance of the CO_2 concentration in the feed, the flow rate of the gaseous feed, the channel length, and the GDE porosity.

5.6 Figures

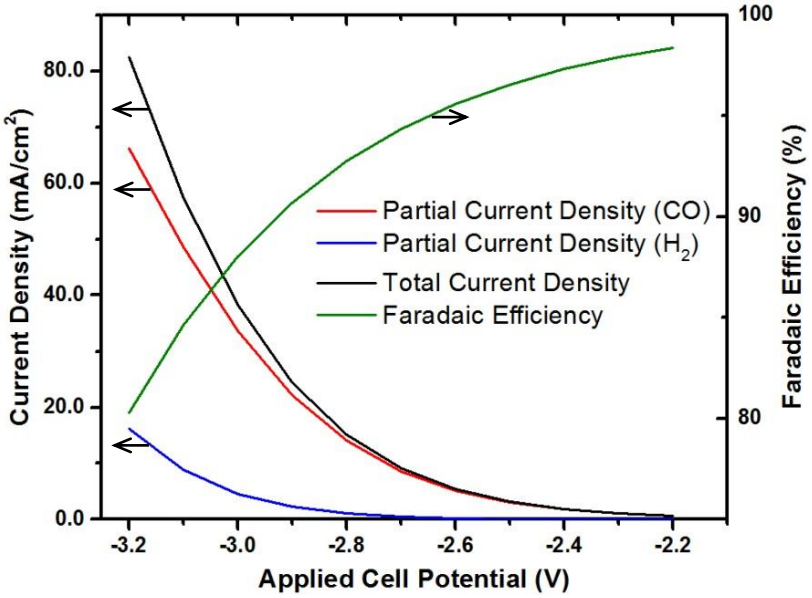

Figure 5.1. Effects of applied cell potential on cell performance. Operating conditions except for cell potential take the base case value in Table 3.1.

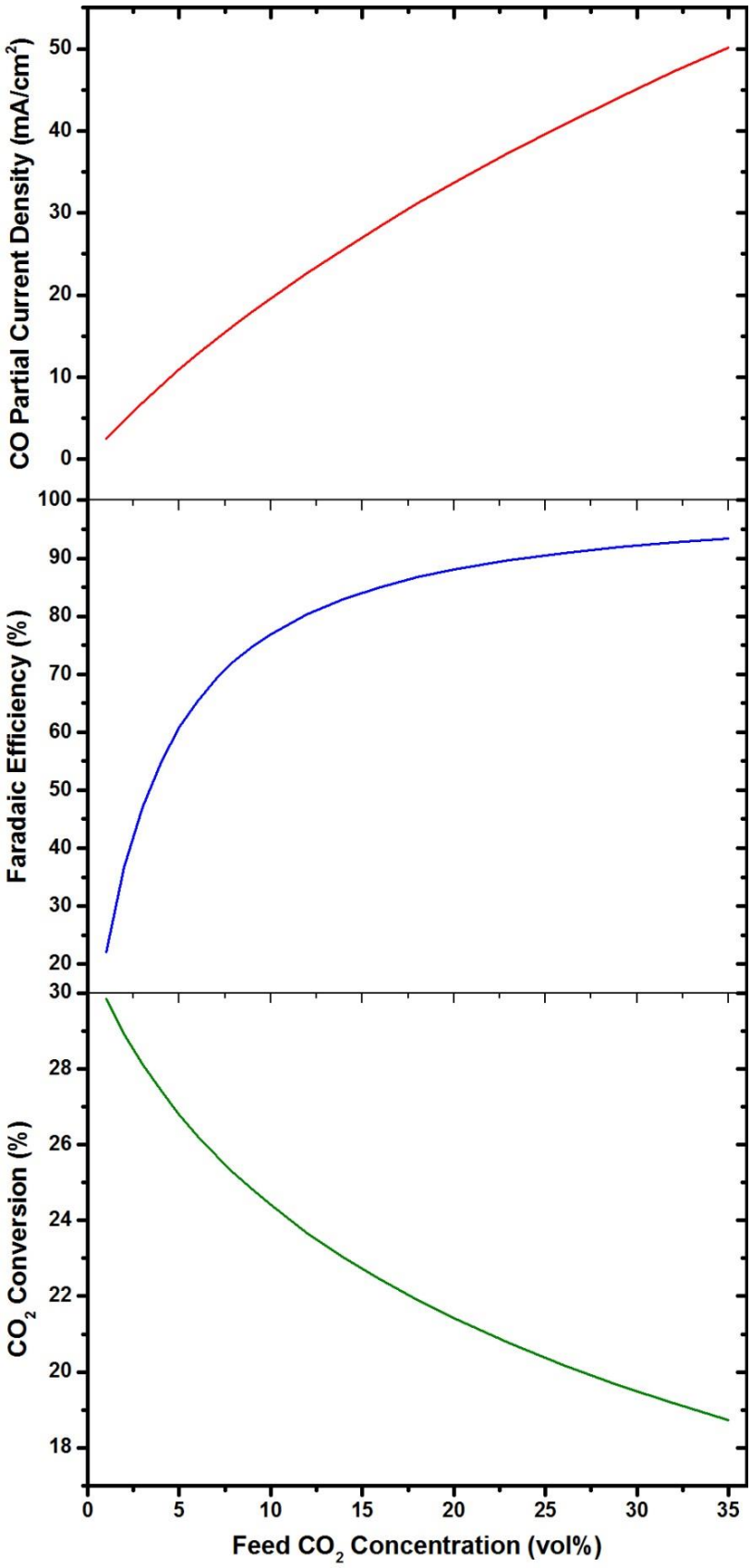

Figure 5.2. Effects of feed CO_2 concentration on cell performance. Operating conditions except feed CO_2 concentration take the base case values in Table 3.1.

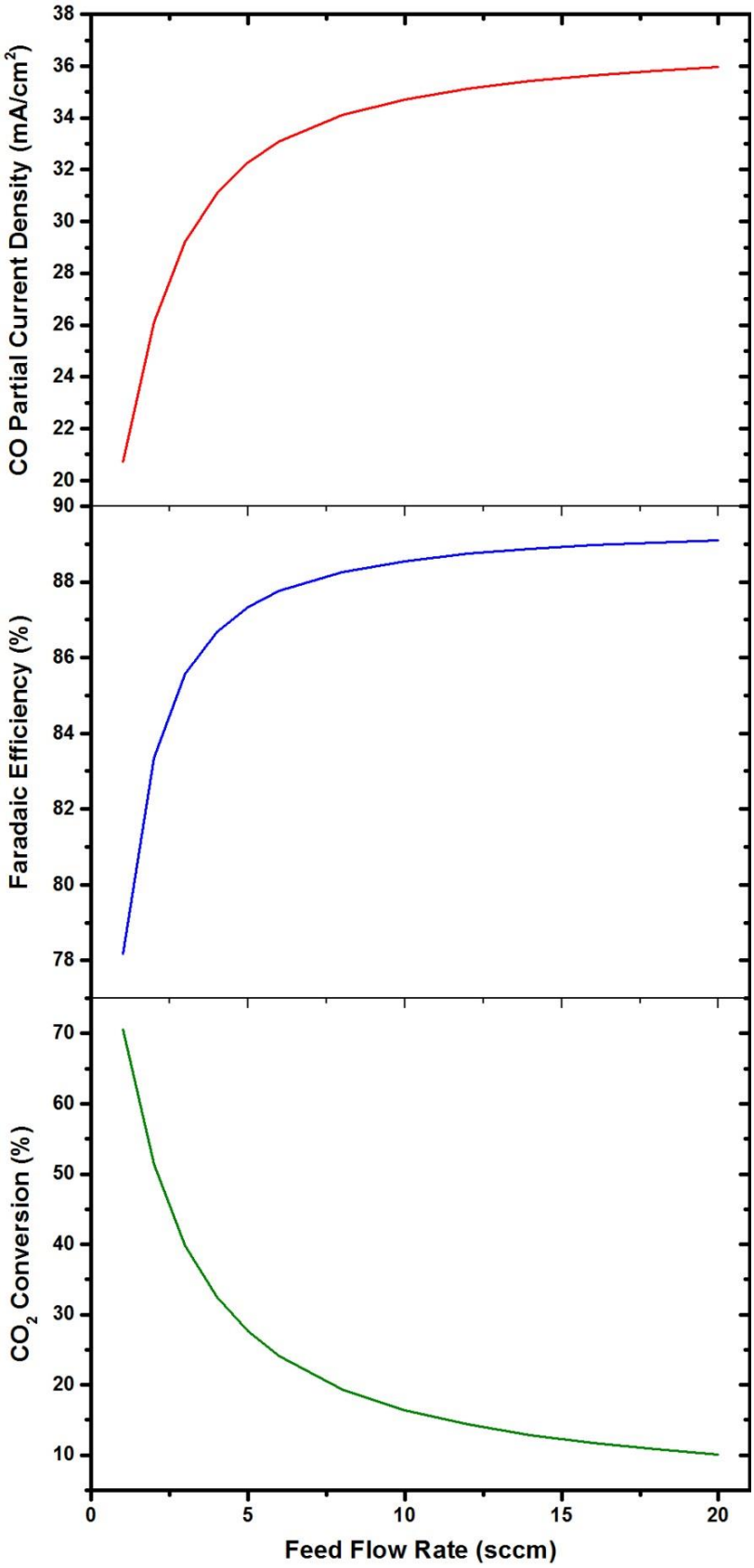

Figure 5.3. Effects of the volumetric flow rate of the gas feed on cell performance. Operating conditions except for feed gas flow rate take the base case values in Table 3.1.

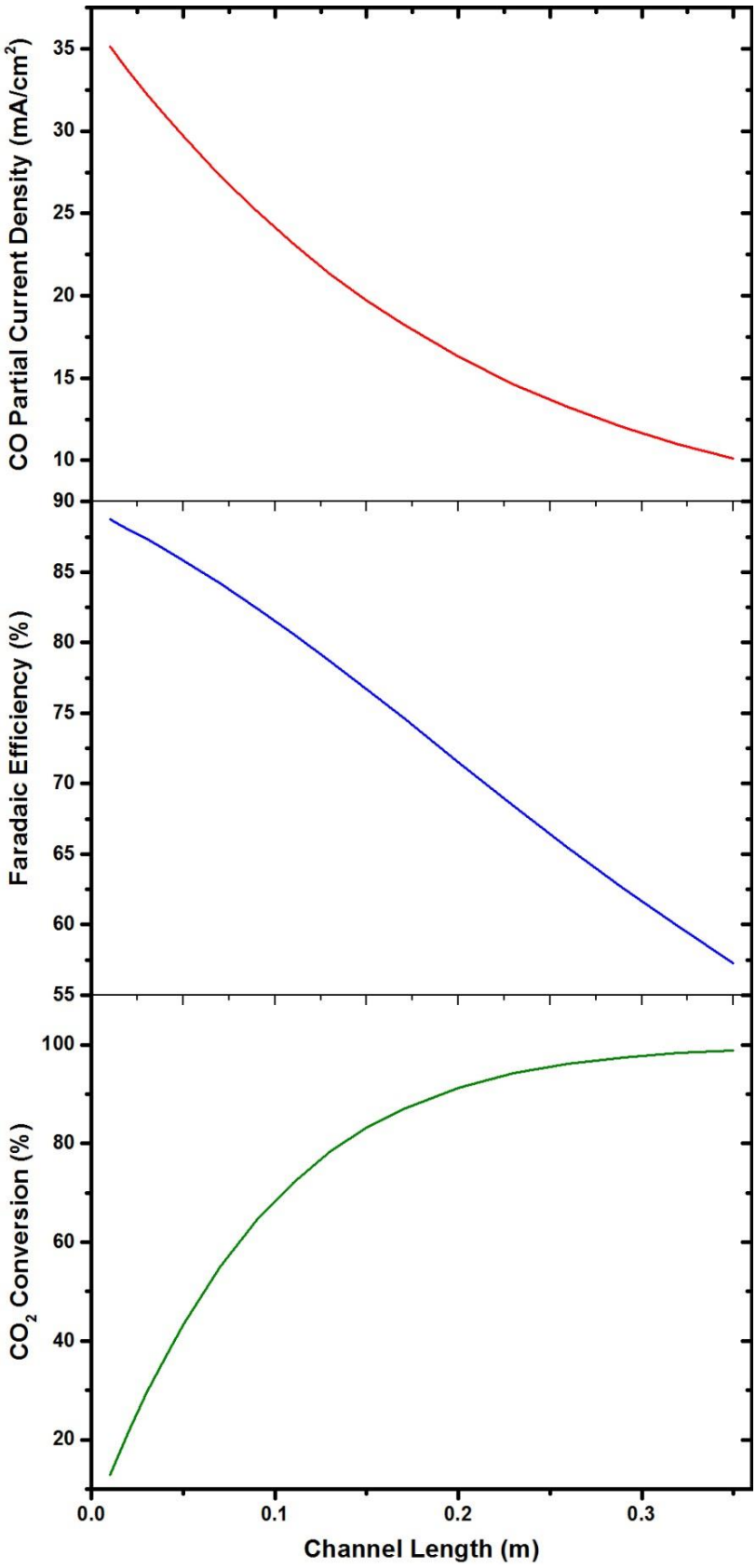

Figure 5.4. Effects of channel length on cell performance. Operating conditions and cell dimensions except for channel length take the base case values in Table 3.1.

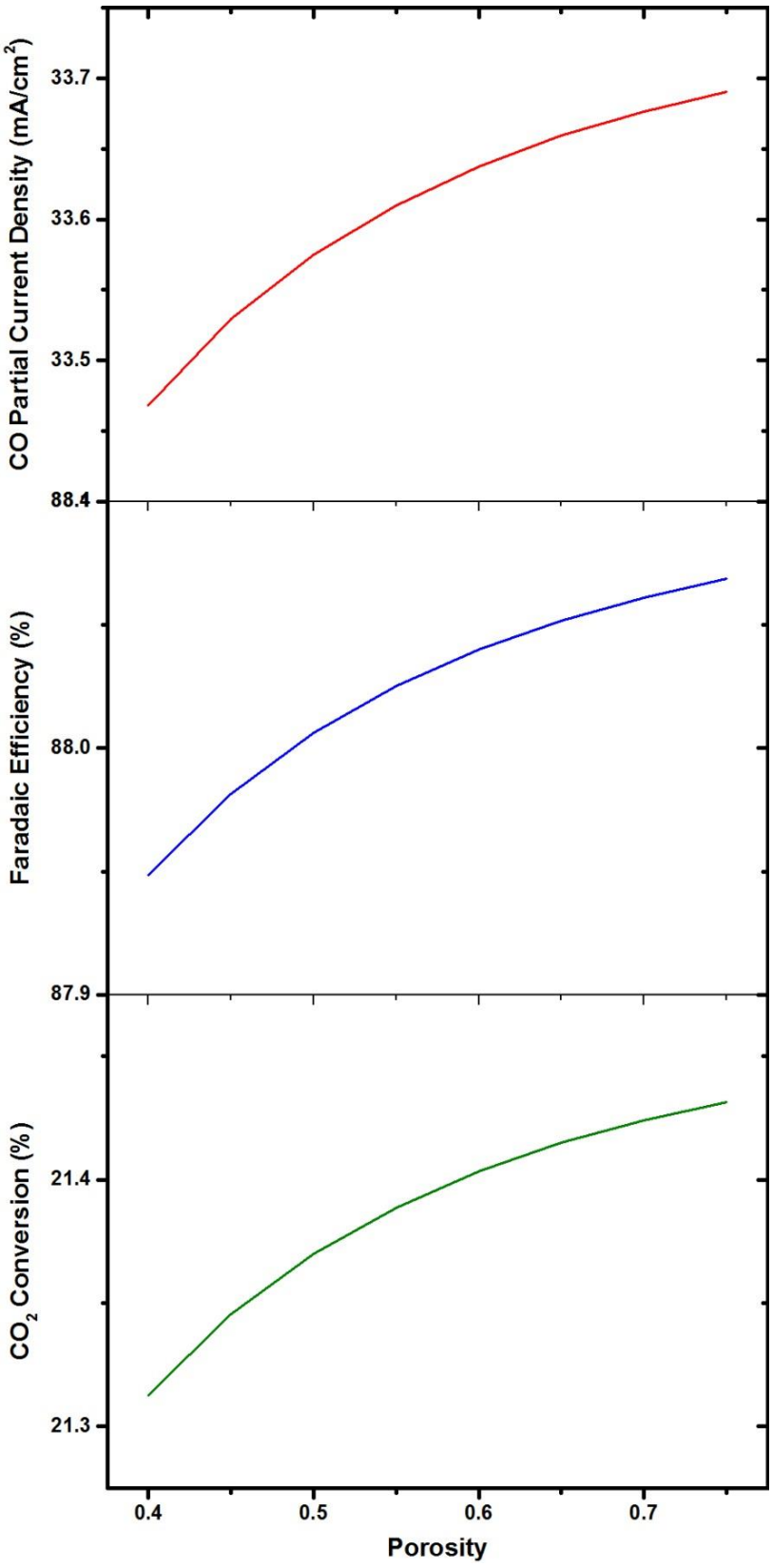

Figure 5.5. Effects of GDE porosity on cell performance. Operating conditions take the base case values in Table 3.1.

CHAPTER 6

REDUCED MODEL FOR A MICROFLUIDIC CELL

6.1 Introduction

In Chapter 3, a detailed mathematical formulation of the electrochemical reduction of CO_2 in a microfluidic cell was presented. Owing to the highly coupled partial differential equations, the detailed model needs to be solved numerically, which can entail significant computational cost and/or complexity. In this chapter, the model is reduced, starting from the full model developed in Chapter 3, in two main steps: (1) a narrow-gap approximation and scaling arguments are used to reduce the complexity of the model formulation; and (2) approximate analytical solutions are obtained by using Taylor-series expansions, homogenization, integration, separation of variables, and Finite Fourier Transforms. Using this approach, a state-space model which is often required in other reduced order model reduction methods yet computationally expensive to derive is not required. The reduced model with approximate analytical solutions will not only reduce the computational time, but also preserve the geometrical resolution and leading order physics. This will not be possible using other model reduction methods. The reduced model is also verified with the experimentally validated full model discussed in Chapter 3.

6.2 Model Reduction for the Catalyst Layers

The catalyst layer has a thickness H_{cl} of about 10 μm and length (L) of greater than or equal to 2 cm, $H_{cl}/L \leq 5 \times 10^{-4} \ll 1$.The slenderness of the catalyst layer allows applying 1D approximation for the catalyst layer. Specifically, the concentration and potential gradient in the catalyst layer (CL) can be assumed to be functions of the distance along the streamwise

direction. Instead of resolving a 2D computational domain, the porous effects and inherent electrochemical reaction kinetics in the catalyst active layers are treated as boundary conditions for the rest of the geometry with a phenomenological expression for the current density. To retain the main features of the catalyst active layer, such as variations in the potential and concentrations, the local current density is still expressed as a function of the electrode potential and CO_2 concentration, as in Eq. (3.25), (3.27) and (3.32).

The simplified schematic is shown in Figure 6.1. The reduced model consists of all the governing equations describing the cathode gas channel, cathode GDL, electrolyte channel, anode GDL and anode gas channel as presented in Chapter 3. All the boundary conditions remain the same except for (VII) cathode CL-electrolyte interface and (VIII) anode CL-electrolyte interface where the electrochemical reactions are taking place.

For the cathode CL-electrolyte interface (VII), the normal mass fluxes of species at this active layer are given by the electrochemical kinetic equations, Eq. (3.25) and Eq. (3.27):

$$\begin{aligned}
\mathbf{n}_{\mathrm{CO_2}} \cdot \mathbf{e}_{\boldsymbol{y}} &= -\frac{i_{\mathrm{CO}}}{2F} M_{\mathrm{CO_2}} \\
\mathbf{n}_{\mathrm{CO}} \cdot \mathbf{e}_{\boldsymbol{y}} &= \frac{i_{\mathrm{CO}}}{2F} M_{\mathrm{CO}} \\
\mathbf{n}_{\mathrm{H_2}} \cdot \mathbf{e}_{\boldsymbol{y}} &= \frac{i_{\mathrm{H_2}}}{2F} M_{\mathrm{H_2}} \\
\mathbf{n}_{\mathrm{H_2O}} \cdot \mathbf{e}_{\boldsymbol{y}} &= -\frac{i_{\mathrm{CO}}}{2F} M_{\mathrm{H_2O}} - \frac{i_{\mathrm{H_2}}}{F} M_{\mathrm{H_2O}}
\end{aligned} \tag{6.1}$$

Transport of species through this interface is specified as a leaking wall with a normal velocity:

$$\mathbf{u}\cdot\mathbf{e}_{\boldsymbol{y}}=\frac{\mathbf{1}}{\rho}\sum_{i}\mathbf{n}_{i}\cdot\mathbf{e}_{\boldsymbol{y}} \qquad i=\mathrm{CO_2, CO, H_2, H_2O} \tag{6.2}$$

The electric potential for this interface is related to the normal current density:

$$\begin{aligned}-\sigma_{\mathrm{elec}}\frac{d\phi_{\mathrm{l}}}{dy}\Big|_{\mathrm{VII_-}}&=\mathbf{i}\cdot\mathbf{e}_{\boldsymbol{y}}\big|_{\mathrm{VII}}\\ -\sigma_{\mathrm{gdl}}\frac{d\phi_{\mathrm{s}}}{dy}\Big|_{\mathrm{VII_+}}&=\mathbf{i}\cdot\mathbf{e}_{\boldsymbol{y}}\big|_{\mathrm{VII}}\end{aligned} \tag{6.3}$$

where the normal current density is described by:

$$\mathbf{i}\cdot\mathbf{e}_{\boldsymbol{y}}\big|_{\mathrm{VII}}=i_{\mathrm{CO}}+i_{\mathrm{H_2}} \tag{6.4}$$

For the anode CL-electrolyte interface (VIII), the normal mass fluxes of species at this active layer are given by the electrochemical kinetic equations, Eq. (3.32):

$$\mathbf{n}_{\mathrm{O_2}}\cdot\mathbf{e}_{\boldsymbol{y}}=-\frac{i_{\mathrm{O_2}}}{4F}M_{\mathrm{O_2}} \tag{6.5}$$

Similar to (VII), the interface condition for electric potential is related to the normal current density:

$$\begin{aligned}-\sigma_{\mathrm{elec}}\frac{d\phi_{\mathrm{l}}}{dy}\Big|_{\mathrm{VIII_+}}&=\mathbf{i}\cdot\mathbf{e}_{\boldsymbol{y}}\big|_{\mathrm{VIII}}\\ -\sigma_{\mathrm{gdl}}\frac{d\phi_{\mathrm{s}}}{dy}\Big|_{\mathrm{VIII_-}}&=\mathbf{i}\cdot\mathbf{e}_{\boldsymbol{y}}\big|_{\mathrm{VIII}}\end{aligned} \tag{6.6}$$

where the normal current density is described by:

$$\mathbf{i} \cdot \mathbf{e_y}\big|_{\text{VIII}} = i_{\text{O}_2} \tag{6.7}$$

To re-calibrate the kinetic parameters (α_{CO}, α_{H_2}, α_{O_2}, $i_{\text{CO,ref}}$, $i_{\text{H}_2\text{,ref}}$ and $i_{\text{O}_2\text{,ref}}$), the CL reduced model was implemented with the updated boundary conditions on COMSOL, and parameter estimation was performed using experimental results described in Chapter 4 on MATLAB with a Livelink to COMSOL.

The results of re-calibration of kinetic parameters are shown in Table 6.1. Figure 6.2 compares the simulated polarization curves obtained using the full model and the CL reduced model with the experimentally measured polarization curves. Good agreement is observed, especially between the two simulation results, where the average percent error is less than 1%. This justifies our reduction for the CL.

6.3 Model Reduction Based on Scaling Analysis

The main idea of scaling analysis is to evaluate the relative importance of the various terms and identify the leading order terms in in the governing equations of a physical process[111]. The remaining terms are treated as smaller corrections and neglected in the reduced model formulation. Similar to analysis performed for fuel cell[112-114], the model formulation will be reduced by exploiting three characteristics of a typical microfluidic flow cell: (1) the slenderness of a typical microfluidic flow cell; (2) the impermeable nature of the GDL as compared to the gas flow channel; and (3) the streamwise-dominant mass transport in the gas flow channel.

Slenderness of a typical microfluidic cell – The height of the gas channel, $H_g \sim O(10^{-3})$ m, and the thickness of the GDL, $H_{gdl} \sim O(10^{-4})$ m, are significantly smaller than the length,

$L \sim O(10^{-1})$ m, i.e. $\frac{H_g}{L} \ll 1, \frac{H_{gdl}}{L} \ll 1$. This allows for a narrow-gap approximation.[95, 114, 115] The second-order diffusive terms in the streamwise direction are negligible at leading order, thus the elliptic PDEs in Eq. (3.4)-(3.7) for the cathode gas channel and (3.11) – (3.15) for the cathode GDL, can be mathematically reduced to parabolic PDEs.

Impermeable nature of the GDL – The GDL of a typical microfluidic cell has a permeability $\kappa \sim O(10^{-12})$ m^2. For $\kappa \leq 10^{-10}$ m^2, the shear stress-induced velocity in the streamwise direction, denoted by u, at the interface between the gas channel and GDL (V in Figure 6.1) is negligible, and hence can be set to zero at leading order.[114, 115] Discarding the shear stress-induced velocity leaves the velocity in the normal direction, v, stemming from the electrochemical reaction in the CL (VII). Species transport equations can be reduced in similar manner. By neglecting the streamwise transport of momentum, mass and species, the parabolic PDEs for GDL can be further reduced to ODEs (1D) in this domain.

Dominant flow in the gas channel – The following dimensionless numbers are considered:

$$\Lambda \equiv \frac{[i][M]}{\rho U_{\mathrm{g,in}} F}\ ,\ \sigma \equiv \frac{H_g}{L}\ ,\ \Omega \equiv \frac{\Lambda}{\sigma} \tag{6.8}$$

where Λ is a Damkohler number, which describes the ratio of the mass flux of the electrochemical reaction to the convective flow and Ω is the modified Damkohler number. $[i]$ is the scale of current density $\sim O(10^3)$ A/m^2; $[M]$ is the scale of molecular mass $\sim O(10^{-2})$ kg/mol; and gas density $[\rho]$ can be estimated from ideal gas law and $[\rho] \sim O(1)$ kg/m^3. With these parameter scales, Ω is calculated to be $\sim O(10^{-2}) \ll 1$. Scaling the governing equations of GDL with Ω and safely neglecting the terms of $O(\Omega)$, the normal velocity $v = 0$ is obtained. Therefore, streamwise transport is dominant in the gas channel.

6.4 Reduced Model Formulation

As there is no crossover of gas species from the anode to the cathode, nor reactions involving anode gas species as a reactant, the transport of species in the anode gas channel and GDL will not affect the performance of the other functional layers in the CO_2 microfluidic electrolyzer. As the interest of this study is on the cathode side where the electrochemical reduction of CO_2 is taking place, the governing equations for the anode (continuity of mass, conservation of momentum and species continuity equations) will not be taken into account in the reduced model formulation. Conservation of charge at the anode is still applied.

Based on the arguments discussed in the previous two sections, the reduced model for the cathode gas channel can now be written as

$$\frac{\partial u}{\partial x} = 0 \tag{6.9}$$

$$\rho u \frac{\partial u}{\partial x} = -\frac{\partial p}{\partial x} + \mu \frac{\partial^2 u}{\partial y^2} \tag{6.10}$$

$$\frac{\partial p}{\partial y} = 0 \tag{6.11}$$

$$\frac{\partial (u\omega_i)}{\partial x} = D_{ij} \frac{\partial^2 \omega_i}{\partial y^2} \qquad i = \mathrm{CO_2, CO, H_2, H_2O} \tag{6.12}$$

and for the cathode GDL

$$\frac{\partial v}{\partial y} = 0 \tag{6.13}$$

$$\frac{\partial p}{\partial y} = -\frac{\mu}{\kappa} v \tag{6.14}$$

$$\frac{\partial (v\omega_i)}{\partial y} = D_{ij}^{\text{eff}} \frac{\partial^2 \omega_i}{\partial y^2} \qquad i = \text{CO}_2, \text{CO}, \text{H}_2, \text{H}_2\text{O} \tag{6.15}$$

and for the electrolyte channel

$$\frac{\partial^2 \phi_{\text{l}}}{\partial x^2} + \frac{\partial^2 \phi_{\text{l}}}{\partial y^2} = 0 \tag{6.16}$$

The boundary conditions for the reduced model are the same as the CL reduced model, except for some redundant terms. To be explicit, the boundary conditions for the reduced model are presented:

At the inlet of the cathode gas channel (I),

$$u = U_{\text{g,in}}, \qquad \omega_{\text{CO}_2} = \omega_{\text{CO}_2,\text{in}}, \qquad \omega_{\text{CO}} = 0, \qquad \omega_{\text{H}_2} = 0, \qquad \omega_{\text{H}_2\text{O}} = 0 \tag{6.17}$$

At the outlet of the gas channel (II),

$$p = p_{\text{exit}} \tag{6.18}$$

At the upper wall of the gas channel (III),

$$u = 0\,, \quad \frac{\partial(\omega_i)}{\partial y} = 0 \qquad i = CO_2, CO, H_2, H_2O \qquad (6.19)$$

At the cathode gas-channel-GDL interface (V), continuity of velocity, pressure, species mass fraction and flux are applied.

Boundary conditions at the left and right walls of the GDL are redundant. Boundary conditions for the reduced model at the cathode CL-electrolyte interface (VII) and anode CL-electrolyte interface are same as those presented in Eqs. (6.1) – (6.7).

6.5 Approximate Analytical Solutions

The derivation of approximate analytical solutions required various symbolic computations using MAPLE 18, which is a general algebra system that supports symbolic computation and visualization[116]. MATLAB codes for the analytical solutions with eigenvalues generated by MAPLE 18 were then exported to MATLAB 2012b without returning to Maple 18.

To secure an approximate analytical solution for the model, the following additional approximations are introduced:

(1) Instead of assuming a weakly compressible flow in the gas channel, incompressible flow is assumed. This assumption holds reasonably well for our systems where the pressure drops is much smaller than the system pressure and the current is small (≤ 100 mA/cm^2).

(2) Instead of using Maxwell-Stefan diffusion model, Fick's diffusion is assumed sufficient and the diffusion coefficients can be treated as constant.

(3) The potential change in the solid phase (the GDL) is insignificant. Electronic conductivity of the solid phase is 5×10^4 S/m while ionic conductivity of the electrolyte is 15 S/m. It is reasonable to assume a negligible Ohmic loss for the solid phase.

Velocities and Pressure – For the cathode gas channel, first substituting Eq. (6.10) into (6.11), noting from (6.12) that p is independent of y, integrating (6.11) twice and applying the boundary conditions (no slip condition, i.e. Eq.(6.19) and continuity/symmetric condition), closed form expressions for the streamwise velocity can be obtained. The pressure drop is related to the mean velocity. The solutions are expressed using the mean inlet velocity:

$$u(y) = 6U_{g,in}\left(\frac{y}{H_g} - \frac{y^2}{H_g^2}\right) \qquad 0 \le y \le H_g \qquad (6.20)$$

$$p(x) = p_{\text{exit}} - \frac{12\mu U_{g,in}}{H_g^2}(x - L) \qquad 0 \le x \le L \qquad (6.21)$$

Note that $\frac{12\mu U_{g,in}}{H_g^2}(x - L) \ll p_{\text{exit}}$.

For the GDL, 1D Equations (6.13) and (6.14) can be integrated together with the boundary conditions (6.1) – (6.2):

$$v = \frac{\mathbf{1}}{\rho}\left(-\frac{i_{\text{CO}}}{2F}\left(M_{\text{CO}_2} + M_{\text{CO}} - M_{\text{H}_2\text{O}}\right) - \frac{i_{\text{H}_2}}{2F}\left(2M_{\text{H}_2\text{O}} - M_{\text{H}_2}\right)\right) \qquad (6.22)$$

$$p(x,y) = p(x,0) - \frac{\mu}{\kappa}vy \qquad -H_{gdl} \le y \le 0 \qquad (6.23)$$

Species Mass Fraction – For the cathode GDL, integrating the 1D species conservation equation Eq. (6.15), while satisfying the two boundary conditions: species continuity and Eq. (6.1), yields

$$\omega_i(x,y) = \omega_i(x,0) + \frac{\mathrm{A}}{\mathrm{B}}(\exp(\mathrm{B}y) - 1) \qquad -H_{gdl} \le y \le 0 \qquad (6.24)$$

where

$$\mathrm{A} = \frac{\left(\rho v \omega_i\left(x,-H_{gdl}\right) - n_i\right)}{\rho \omega_i\left(x,-H_{gdl}\right)\exp\left(-\frac{vH_{gdl}}{D_{ij}^{\mathrm{eff}}}\right)} \text{ and } \mathrm{B} = \frac{v}{D_{ij}^{\mathrm{eff}}} \qquad (6.25)$$

v is defined in Eq. (6.22) and $n_i = \mathbf{n}_i \cdot \mathbf{e}_{\boldsymbol{y}}$ is defined in Eq. (6.1). To secure an explicit expression that does not require a numerical scheme to solve, $\omega_i\left(x,-H_{gdl}\right)$ need to be determined. Eq. (6.25) is evaluated at $y = -H_{gdl}$,

$$f\left[\omega_i\left(x,-H_{gdl}\right)\right] \equiv \omega_i\left(x,-H_{gdl}\right) - \omega_i(x,0) - \frac{\mathrm{A}}{\mathrm{B}}\left(\exp\left(-\mathrm{B}H_{gdl}\right) - 1\right) = 0 \qquad (6.26)$$

Introducing a Taylor-series expansion of $f\left[\omega_i\left(x,-H_{gdl}\right)\right]$ about $\omega_i(x,0)$ at $y = 0$ gives

$$f\left[\omega_i\left(x,-H_{gdl}\right)\right] \approx f[\omega_i(x,0)] + f'[\omega_i(x,0)]\Delta\omega_i + \frac{1}{2}f''[\omega_i(x,0)]\Delta\omega_i^2 + O(\Delta\omega_i^3) \qquad (6.27)$$

where $\Delta\omega_i = \omega_i\left(x,-H_{gdl}\right) - \omega(x,0)$, and $f'[\omega_i(x,0)]$, $f''[\omega_i(x,0)]$ are the first and second derivatives of $f[\omega_i(x,y)]$ with respect to $\omega_i(x,y)$ evaluated at $y = 0$. Assuming that a first order Taylor expansion is sufficiently accurate,

$$\omega_i(x, -H_{gdl}) \approx \omega_i(x,0) - \frac{f[\omega_i(x,0)]}{f'[\omega_i(x,0)]} \tag{6.28}$$

and now $A \equiv A[\omega_i(x,0)]$. Substituting Eq. (6.28) into Eq. (6.24) leads to an approximate analytical solution for the species mass fractions in the GDL, provided that $\omega_i(x,0)$ is available.

For the cathode gas channel, the species conservation equation Eq. (6.12) is a linear parabolic PDE that can be solved by separation of variables, provided that the boundary conditions are linear and homogeneous. In this case, all the boundary conditions fulfil these criteria except at the interface between the gas channel and the GDL (V in Figure 6.1) ($y = 0$), where the boundary condition from flux continuity can be written as

$$\left.\frac{\partial \omega_i}{\partial y}\right|_{y=0_+} = \varepsilon^{1.5} \left.\frac{\partial \omega_i}{\partial y}\right|_{y=0_-} \tag{6.29}$$

where the right hand side can be obtained by differentiating Eq. (6.24) at $y = 0$, resulting in

$$\left.\frac{\partial \omega_i}{\partial y}\right|_{y=0_+} = \varepsilon^{1.5} A \tag{6.30}$$

where $A = f\left[\omega_i(x, -H_{gdl})\right] \approx f[\omega_i(x,0)]$.

The linear and homogeneous system of equations now can be solved with separation of variables,

$$\omega_i = \sum_{k=1}^{\infty} c_k \exp\left(-\frac{D_{ij}}{U_{g,in}}\lambda_k^2 x\right)\left(\frac{\varepsilon^{1.5}}{\lambda_k}\sin(\lambda_k y) + \cos(\lambda_k y)\right) \tag{6.31}$$

The Fourier coefficients c_k and the eigenvalues λ_k are obtained using Maple 18 as follows:

$$c_k = \frac{2\omega_{i,\text{in}}\lambda_k\varepsilon^{1.5}\left[\left(1-\cos\left(\lambda_k H_g\right)\right) + \lambda_k \sin(\lambda_k H_g)\right]}{\varepsilon^{1.5}\left(\lambda_k H_g - \Gamma\right) - 2\varepsilon^{1.5}\lambda_k\left(1+\cos\left(\lambda_k H_g\right)^2\right) + \lambda_k^2(\Gamma + \lambda_k H_g)} \tag{6.32}$$

$$\tan\left(\lambda_k H_g\right) = \varepsilon^{1.5}/\lambda_k \tag{6.33}$$

where $\Gamma = \sin\left(\lambda_k H_g\right)\cos(\lambda_k H_g)$.

Electric Potential in the Electrolyte – To solve the Eq. (6.16) with boundary conditions, Finite Fourier Transform method is applied. As charge insulations is assumed, the left and right boundary ($x = 0$ & $x = L$) are homogeneous Neumann boundary conditions. For the top and bottom ($y = -H_{gde}$ & $y = -H_{gde} - H_{elec}$), noting that the local current densities are dependent on x only, these boundary conditions can be treated as nonhomogeneous Neumann boundary. Basis functions involving x are selected and the overall solution is

$$\begin{aligned}\phi_l(x,y) = \sum_{m=1}^{\infty} \frac{1}{sinh\left(\frac{m\pi H_{elec}}{L}\right)}\Bigg[&\Delta_m \sin\left(\frac{\left(m+\frac{1}{2}\right)\pi x}{L}\right)\cosh\left(\frac{m\pi y}{L}\right) \\ &+ \mathrm{E}_m \sin\left(\frac{\left(m+\frac{1}{2}\right)\pi x}{L}\right)\left(\cosh\left(\frac{\left(m+\frac{1}{2}\right)\pi x}{L}\right)\sinh\left(\frac{m\pi H_{elec}}{L}\right)\right. \\ &\left.- \cosh\left(\frac{m\pi H_{elec}}{L}\right)\sinh\left(\frac{m\pi y}{L}\right)\right)\Bigg]\end{aligned} \tag{6.34}$$

where Δ_m and E_m are constants evaluated from the nonhomogeneous conditions, using the following equations:

$$\Delta_m = \sqrt{\frac{2}{L}} \int_0^L \left(\left. \frac{d\phi_l}{dy} \right|_{y=-H_{gdl}-H_{elec}} \right) \cos\left(\frac{\left(m+\frac{1}{2}\right)\pi x}{L} \right) dx \tag{6.35}$$

$$\mathrm{E}_m = \sqrt{\frac{2}{L}} \int_0^L \left(\left. \frac{d\phi_l}{dy} \right|_{y=-H_{gdl}} \right) \sin\left(\frac{\left(m+\frac{1}{2}\right)\pi x}{L} \right) dx \tag{6.36}$$

The local potential gradients are related to local current densities using Ohm's law, Eq. (3.21) and solved using the electrochemical kinetic equations, Eqs. (3.25), (3.27) and (3.32).

6.6 Validation and Analysis

To verify the accuracy of the approximate analytical solutions derived in the previous section for the velocities, pressure and species mass fractions in the cathode gas channel and cathode GDL, and electric potential in the electrolyte, the approximate analytical solutions are compared with the numerical solutions obtained in Chapter 3 for the base case parameter values presented in Table 3.1.

Accuracy of approximation using Taylor expansion – Recall that in deriving the analytical solutions for the species mass faction in GDL, only the first-degree terms in the Taylor-series expansion for $\omega_i\left(x, -H_{gdl}\right)$ are retained. To ensure that the approximate solution is valid, the expression for $\omega_{CO_2}\left(x, -H_{gdl}\right)$ in Eq. (6.25) is compared with the numerical solutions at various CO_2 mass fractions, as shown in Figure 6.3. Good agreement is observed for $H_{gdl} = 1 \times 10^{-4}$ m and 3×10^{-4} m. As expected, the accuracy decreases with an increase in H_{gdl}. However, even at $H_{gdl} = 10^{-3}$ m which is 1 order of magnitude

larger than commercial GDL[102], the maximum relative error is only 3%. In conclusion, a first-order Taylor-series expansion is sufficient for the considered operating conditions and geometry parameters.

Verification of species mass fractions – The mass fractions of CO_2 across the cathode gas channel and cathode GDL, under the base case operating and design conditions, as predicted from the approximate analytical solutions and their numerical counterparts are shown in Figure 6.4; while the same comparisons for CO are shown in Figure 6.5. The approximate analytical solutions are able to reproduce the local CO_2 distributions in both the gas channel and the GDL reasonably well, with a maximum relative error of 5%. As for the CO distributions, the fitting is not as good, with a maximum relative error of 15%. However, this relative error is understandable given the relatively small magnitude of the CO mass fraction. From Figure 6.4 and Figure 6.5, it is also clear that the approximate analytical solution is capable of capturing not just the trends of change, but also the boundary behaviors near the catalyst active layer.

Verification of polarization curves – The performance of the approximate analytical solutions is further analyzed by considering the electrochemical performance. Figure 6.6 compares polarization curves obtained at four different channel lengths as predicted using the approximate analytical solutions and from numerical solutions of the full model. Good agreement with average relative error < 2% is observed. Fitting improves as channel length increases from $L = 2$ cm to $L = 20$ cm. This is expected as an increase in channel length implies smaller residual errors being neglected in the scaling analysis based on the narrow-gap approximation.

Computational efficiency – Table 6.2 shows the comparison of computational time from Matlab and COMSOL respectively for the reduced model with approximate analytical

solutions and the full model on a PC with Intel® Core™ i7-3770 CPU @ 3.40 GHz PC with 16.0 GB RAM. Time recorded in MATLAB is by using *tic* and *toc* MATLAB functions while the time recorded in COMSOL is from COMSOL solution report. It is obvious that the reduced model with approximate analytical solutions takes significantly less time to solve for one run of simulation.

6.7 Conclusions

In this chapter, a reduced model with approximate analytical solutions for a steady state and isothermal 2D model for the electrochemical reduction of CO_2 is presented. The reduced model with approximate analytical solutions has been verified with the experimentally validated full model. Good agreements between the reduced model and the full model are observed for species distributions and polarization curves. The reduced model with approximate analytical solutions requires only a few seconds to solve one run of simulation. With such an efficient and effective model, the unit cell model can be suitably extended to cell stack model. Formulation of the cell stack model using the current unit cell models as building block will be discussed in the next chapter.

6.8 Figures

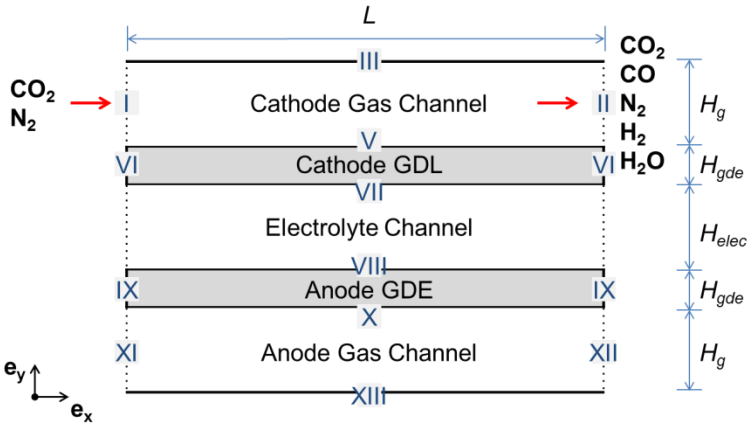

Figure 6.1. Simplified schematic used in the reduced model formulation. Boundaries are marked with Roman numerals: (I) cathode gas channel inlet; (II) cathode gas channel outlet; (III) cathode gas channel horizontal wall; (V) cathode gas-channel-GDL interface; (VI) cathode GDE vertical walls; (VII) cathode CL-electrolyte interface; (VIII) anode CL-electrolyte interface; (IX) anode GDE vertical walls; (X) anode gas-channel-GDL interface; (XI) anode gas channel wall/inlet; (XII) anode gas channel wall/outlet; (VIII) anode gas channel wall/opening. (IV) is neglected to keep the numbering consistent with Figure 3.1.

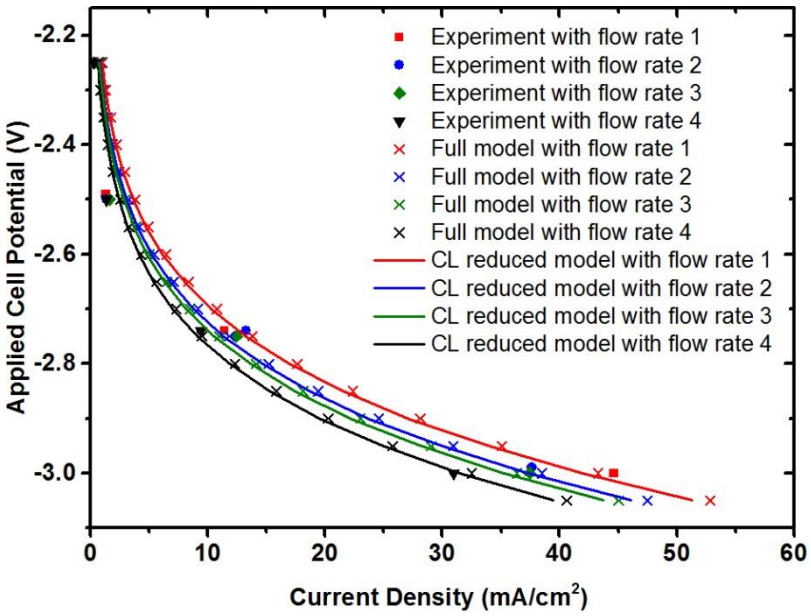

Figure 6.2. Comparison of polarization curves for re-calibration on kinetic parameters using the CL reduced model. Feed gas flow rates and compositions are specified in Table 4.1. Other operating conditions take the base case values in Table 3.1.

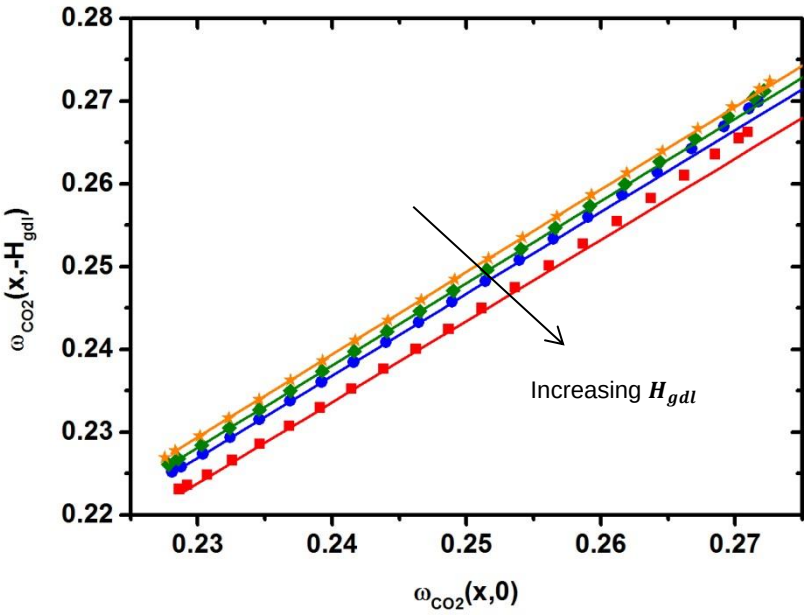

Figure 6.3. Mass fraction of CO_2 at the CL-electrolyte interface $\omega_{CO2}(x,-H_{gdl})$ as a function of mass fraction of CO_2 at the cathode gas-channel-GDL interface $\omega_{CO2}(x,0)$. Comparison between numerical solutions (symbols) and analytical solutions (solid lines) for the GDL thickness: $H_{gdl} = 1 \times 10^{-4}$, 3×10^{-4}, 5×10^{-4} and 1×10^{-3} m. Other operating conditions take the base case values in Table 3.1.

(a)

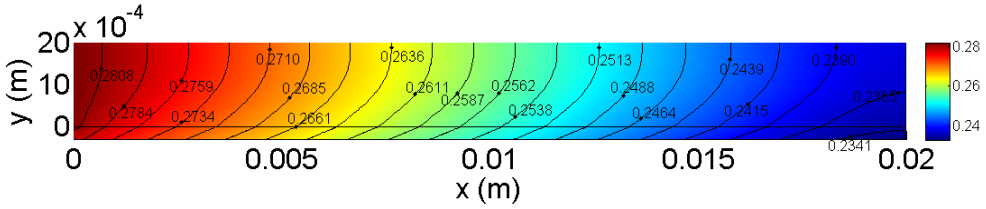

(b)

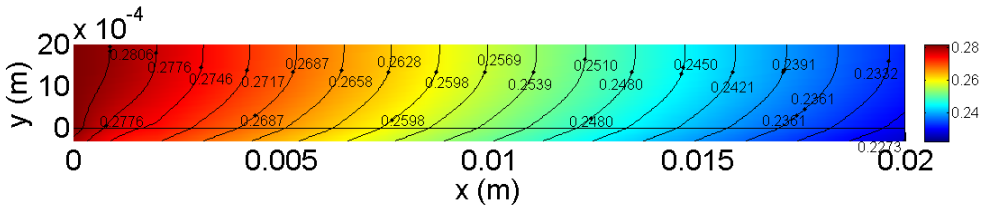

Figure 6.4. CO_2 mass fractions in the cathode gas channel and cathode GDL for the base case: (a) numerical solution of the full model; and (b) approximate analytical solution. The horizontal lines in the above plots separate the cathode gas channel from cathode GDL. Operating conditions take the base case values in Table 3.1.

(a)

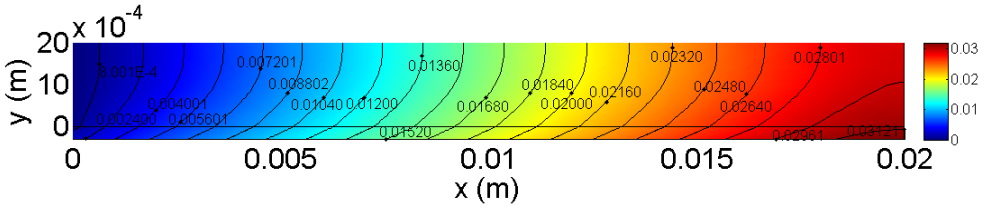

(b)

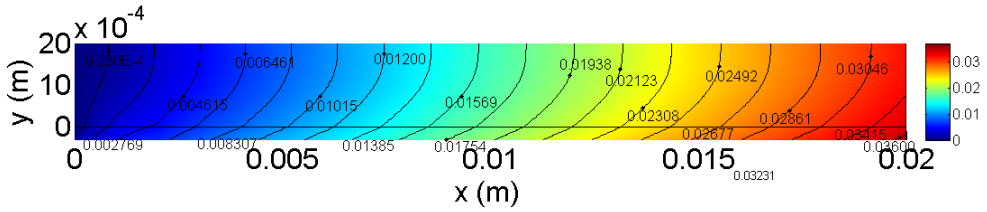

Figure 6.5. CO mass fractions in the cathode gas channel and cathode GDL for the base case: (a) numerical solution of the full model; (b) approximate analytical solution. The horizontal lines in the above plots separate the cathode gas channel from cathode GDL. Operating conditions take the base case values in Table 3.1.

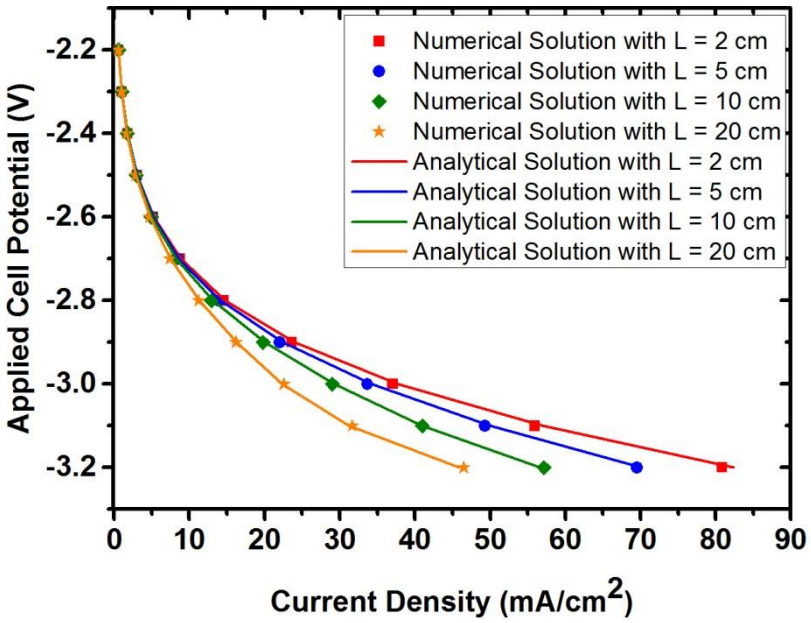

Figure 6.6. Comparison of polarization curves for validation of analytical solutions with numerical solutions with different channel lengths. All the other operating conditions take the base case values in Table 3.1.

6.9 Tables

Table 6.1. Parameters in the electrochemical reaction kinetic equations for the reduced model formulation

Parameter	Symbol	Value	Unit
Reversible potential of CO formation half-cell	E_{CO}	–0.52	V (at pH 7 vs SHE)
Reversible potential of H_2 formation half-cell	E_{H2}	0.41	V (at pH 7 vs SHE)
Reversible potential of O_2 formation half-cell	E_{O2}	0.82	V (at pH 7 vs SHE)
Reference CO_2 concentration	$C_{\mathrm{CO_2,ref}}$	40.9	mol/m^3
Exchange current density	$i_{\mathrm{CO,\,ref}}$	2.57×10^{5}	A/m^2
Exchange current density	$i_{\mathrm{H_2,\,ref}}$	9.67×10^{-4}	A/m^2
Exchange current density	$i_{\mathrm{O_2,\,ref}}$	1.99×10^{-6}	A/m^2
Charge transfer coefficient of CO formation half-cell	α_{CO}	0.17	-
Charge transfer coefficient of H_2 formation half-cell	$\alpha_{\mathrm{H_2}}$	0.25	-
Charge transfer coefficient of O_2 formation half-cell	$\alpha_{\mathrm{O_2}}$	0.79	-

Table 6.2. Comparisons of computational time for one run of simulation using the full model and using the reduced model with approximate analytical solutions. All design and operating conditions except channel length L take their base case values in Table 3.1.

Case	**L = 2 cm**	**L = 5 cm**	**L = 10 cm**	**L = 20 cm**
Full model solutions	8 min	10 min	15 min	17 min
Analytical solutions	2 s	2 s	3 s	4 s

CHAPTER 7

MODELING OF MICROFLUIDIC CELL STACKS

7.1 Introduction

Similar to fuel cell, a number of microfluidic cells can be stacked together for the electrochemical reduction of CO_2 in order to achieve the necessary high throughput for CO_2 conversion. Ideally, each individual cell in the stack will be exposed to identical or close to identical operating conditions to avoid non-uniformities between cells, which can result in a decreased stack performance, reliability, and/or durability. Typical non-uniformities between cells can arise in current and potential distributions between cells, in the flow distribution at the cell inlets due to external manifold design, in the temperature distribution and uneven clamping pressure. Mathematical modeling of a microfluidic cell stack is necessary to understand the essential phenomena that occur within the cell stack. In this chapter, the full model developed in Chapter 3 and the reduced model with approximate analytical solutions developed in Chapter 6 will be employed as the building block for a stack model, and subsequently two mathematical models comprising of the two building block models can be proposed for the electrochemical reduction of CO_2 in a microfluidic cell stack.

7.2 Model Formulation

A 2D microfluidic cell stack comprising of *n* cells as illustrated in Figure 7.1 is considered. The building block is a unit cell that consists of the following parallel and rectangular layers/channels of identical lengths and widths and various heights, from top to bottom, a cathode gas channel, a cathode gas diffusion layer (GDL), an aqueous electrolyte channel, and an anode gas diffusion electrode and an anode gas channel. The cells in the

stack are connected via impermeable graphite or metallic plates which also serve as current collectors. The GDL are coated with suitable catalysts on the sides of the electrolyte channel to provide a three-phase interface for electrochemical reactors. The stack is decoupled from the external manifolds by assigning the inlet velocities for the gas channels, as the focus of the study is with the stack itself and not the external manifolds or auxiliary equipment such as compressors.

Since the cells in a stack are connected via impermeable graphite or metallic plates, transport of mass, momentum and species is confined to the individual cells; in contrast, the transport of charge occurs across the cells and throughout the entire stack. The governing equations for transport of mass, momentum, species and charge in different functional layers in the entire stack remain the same as that for the unit cell. Boundary conditions for the conservation of mass, momentum and species equations for different functional layers remain the same, but with a translation in the direction of stacking, i.e. for functional layers in the j^{th} cell, i.e.

$$(x, y) \rightarrow (x, y - (j-1) \times H_{cell}) \tag{7.1}$$

where H_{cell} is the height of a unit cell. However, for boundary conditions of the conservation of charge equation, continuity of charge is applied for the interfaces between cells, and only at the upper and bottom layer of the stack, applied stack cathode and anode potentials are assigned, i.e.

$$\phi_s|_{\mathrm{III}} = V_{\mathrm{cath}} \quad \text{and} \quad \phi_s|_{\mathrm{XIII}} = V_{\mathrm{anod}} \tag{7.2}$$

The full set of governing equations, considering the conservation of mass, momentum, species and charge in the CO_2 microfluidic electrolyzer, are presented in Chapter 3, Eq. (3.4) – (3.24). The reduced governing equations preserving the leading order physics are presented in Chapter 6, Eq. (6.9) – (6.16), with approach to secure approximate analytical solutions discussed in Section 6.5.

7.3 Numeric and Symbolic Computation

The model with a full set of governing equations as presented in Chapter 3 is formulated in COMSOL Multiphysics. To extend a unit cell model to an *n*-cell stack, a unit cell geometry with the corresponding physics is first formulated, and subsequently the unit cell formulation is transformed using a rectangular array of x size $= 1$ and y size $= n$. The stack model is then solved numerically using finite element method with COMSOL 4.3b. As discussed in Chapter 3, mesh independence is ensured.

Symbolic computations for the approximate analytical solutions are carried out with MAPLE 18 to generate MATLAB code. Velocities, pressure and species mass fractions are first solved for $j = 1$ and translated in the y direction to obtain expression for $2 \leq j = n$. Electric potential is then solved for the entire stack. Post-processing of the analytical solutions from MAPLE is performed in MATLAB 2012b.

7.4 Verification for Stacks with Uniform Flow Distribution

The reduced model with approximate analytical solutions is obtained from the model with a full set of governing equations via model reduction based on scale arguments and mathematical approximation. The reduced model is first verified with the full model, to ensure that it captures the leading-order behavior of the system. For this purpose, uniform inlet conditions are assumed to for every cell in the stack, and the predicted global

polarization curves for a 5-cell stack from the full model and the reduced model are compared. The base case parameters are shown in Table 3.1 with a change in channel length to 0.1 m. As shown in Figure 7.2, good agreement is found throughout the entire polarization curve, with a slight deviation at higher stack potentials. The average relative error is 2% while the maximum relative error is 8% for the entire curve. Good agreement between the reduced model with approximate analytical solutions and the full model suggests that the leading order phenomena has been well resolved.

Distributions of the electric potentials in the solid phase and the electrolyte phase along are compared. Figure 7.3 depicts the distributions at a cross section in the middle of the 5-cell stack at an overall stack potential, V_{stack}, of −15 V. Good agreement between the full model and the reduced model with approximate analytical solutions, once again assures that the leading order physics have been captured by the reduced model. The potential profiles of each individual cell are also identical, with a constant drop of −3 V across each individual cell. Uniform distribution of the cell stack potential among the individual cell is observed when the cell stack is operated at uniform inlet conditions. For brevity, comparisons of other dependent variables such as mass fractions of species and gas flow velocities are not shown here, but the same uniformity can be observed.

7.5 Verification for Stacks with Non-Uniform Flow Distribution

While the reduced model with approximate analytical solutions agrees well with the full model when every cell is operated at identical inlet conditions, the performance of the models when the cell stack is subjected to disturbance is subsequently verified. A leading order flow profile for the inlet velocities at the cathodes for a 5-cell stack is introduced:

$$U_{g,in}(j) = U_{g,in}(1) + (j-1)\Delta U \tag{7.3}$$

where j denotes the number of the cell in the stack (see Figure 7.1), $U_{g,in}(j)$ is the inlet velocity at cell j, and ΔU is the incremment in the inlet velocity from cell to cell. ΔU is chosen to be 20% of the $U_{g,in}$ which is larger than the typical variation in inlet velocities between 5% and 25% that have been studied for U- and Z-shaped external manifolds of fuel cell stacks comprising of 25 to 100 cells[117-119]. As shown in Figure 7.2, good agreement between the global polarization curves obtained from the full model and the reduced model is observed even in this case with non-uniform inlet velocities. The average relative error of 3% and the maximum relative error of 9% for the global polarization curve corresponding to the case with non-uniform inlet flow distribution are only slightly larger than that in the case with identical inlet flow.

Instead of identical channel performance, performance at each individual cell varies in the case with non-uniform inlet flow. With the same defined flow distribution, local current density distribution for a 5-cell stack with V_{stack} of −15 V, corresponding roughly to around −3 V for each cell which is a typical operating potential for CO_2 electrolyzers, is investigated. As illustrated in Figure 7.4, there is a re-distribution of the current densities across the cell stack. The reduced model still agrees well with the full model, with less than 2% error relative to the full model.

7.6 Computational Cost and Efficiency

Computational time taken for solving the full model and the reduced model with approximate analytical solutions for *n*-cell stacks operated with V_{stack} of $-3n$ V with uniform inlet floe distribution, using the same Intel® Core™ i7-3770 CPU @ 3.40 GHz PC with 16.0

GB RAM, are compared in Table 7.1. It is obvious that the approximately analytical solutions take significantly less time to solve for one run of simulation.

The time taken to obtain the numerical solutions of the full model increases tremendously with an increase in the number of cells in the cell stack, while this increase is not that obvious in the case of reduced model with approximate analytical solutions. However, symbolically solving for the expression of the analytical solutions takes significant time and effort, yet this has not been taken into consideration in this comparison.

7.7 Conclusions

In this chapter, two microfluidic cell stack models are presented: (1) a full model that accounts for the transport of species and charges, conservation of momentum and mass, and electrochemical reaction kinetics, in which the full model formulated in Chapter 3 is employed for the building block; and (2) a reduced model with approximate analytical solutions that captures the leading order physics, in which the approach to obtain the approximate analytical solutions based on scaling argument and further mathematical approximations from the full model as discussed in Chapter 6 is adopted. The reduced model has been verified with the full model by comparing the approximate analytical solution with the numerical solutions, both for the case when the cell stack has identical inlet conditions for every cell, and when the cell stack is subjected to a non-uniform flow profile of the cathode inlet velocities. Good agreements are observed for the global polarization curves and local current density distributions at the electrode-electrolyte interface. Overall, the reduced model is effective in capturing the leading order physics and much more computationally efficient as compared to the full model.

7.8 Figures

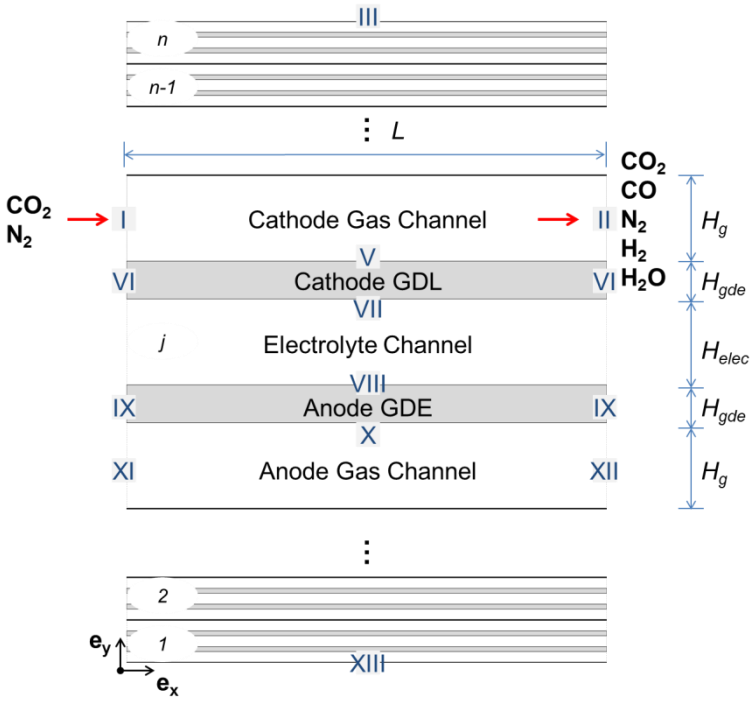

Figure 7.1. Schematic of a microfluidic cell stack comprising of *n* building blocks (denoted by *j*). Boundaries are marked with Roman numerals: (I) cathode gas channel inlets; (II) cathode gas channel outlet; (III) cathode gas channel horizontal wall/cathode current collector; (V) cathode gas-channel-GDL interface; (VI) cathode GDE vertical calls; (VII) cathode CL-electrolyte interface; (VIII) anode CL-electrolyte interface; (IX) anode GDE vertical walls; (X) anode gas-channel-GDL interface; (XI) anode gas channel wall/inlet; (XII) anode gas channel wall/outlet; (VIII) anode gas channel wall/anode current collector. (IV) is neglected to keep the numbering consistent with Figure 3.1.

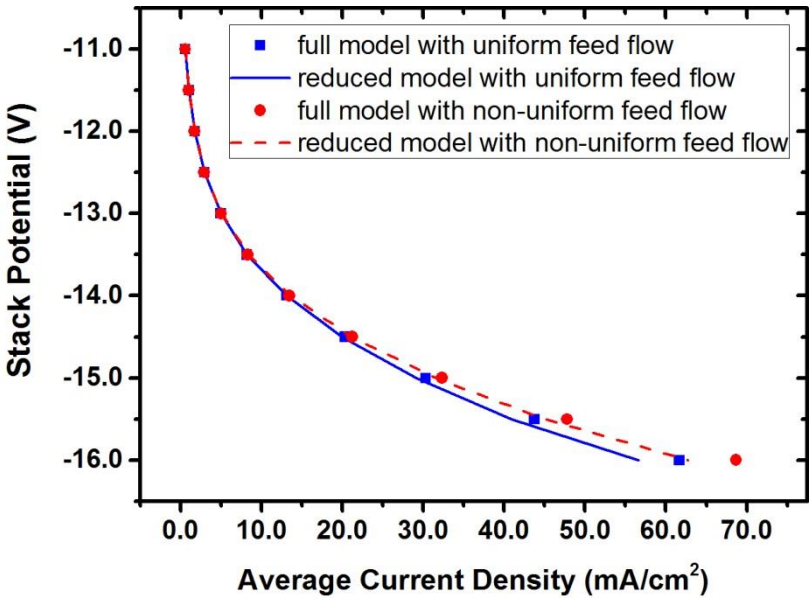

Figure 7.2. Polarization curve for uniform inlet conditions and for non-uniform cathode inlet velocity. Channel Length L = 0.10 m. All the other design and operating conditions take the base case values in Table 3.1.

(a)

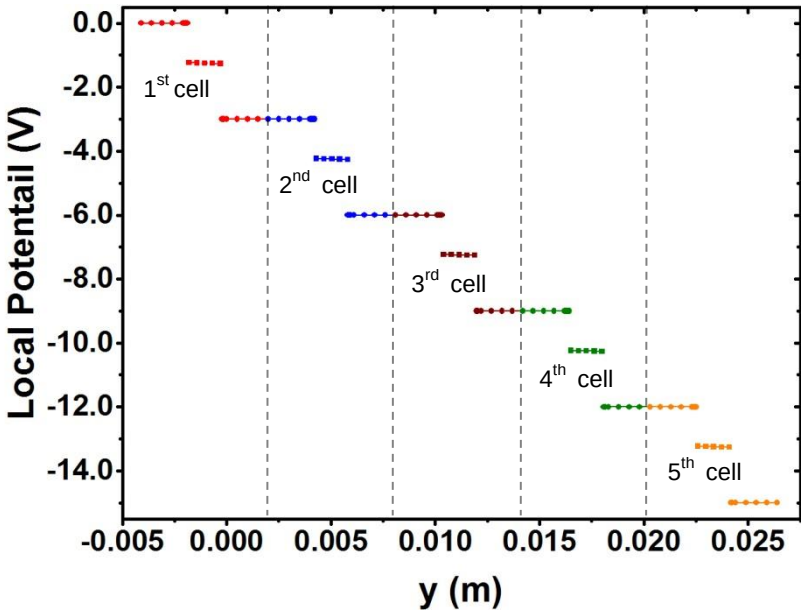

(b)

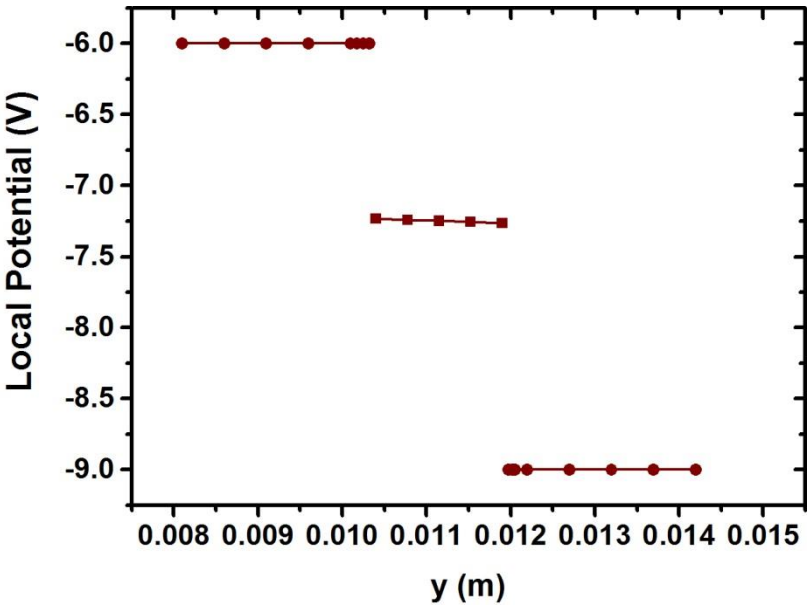

Figure 7.3. Local potential distribution of the solid phase (●) and ionic phase (■) for the full model and the corresponding reduced model with approximate analytical solutions (−) at (a) a cross section ($x = L/2$, $0 \le y \le H_{stack}$ and (b) a close-up of cell 3 at the same cross section, for a 5-cell stack operating at $V_{stack} = -15$ V. Channel Length $L = 0.10$ m. All the other design and operating conditions take the base case values in Table 3.1.

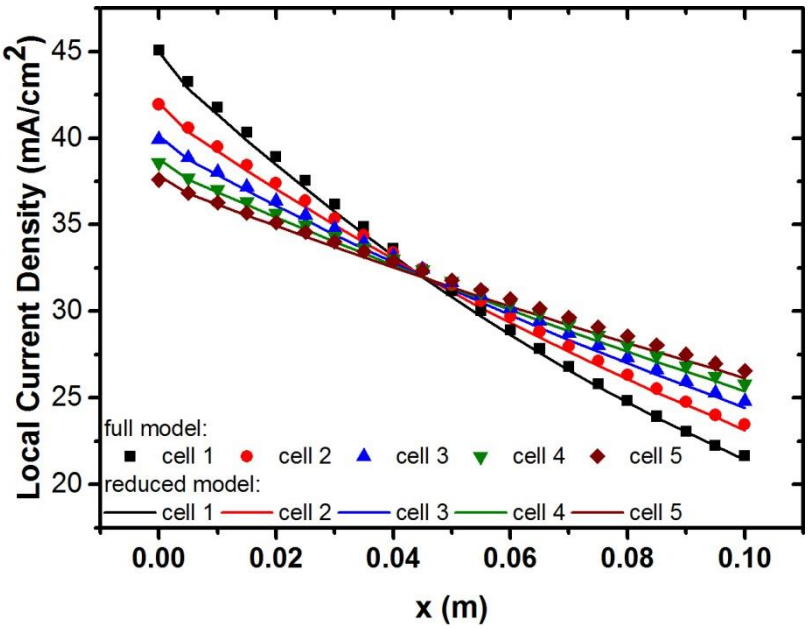

Figure 7.4. Local current density distribution for a 5-cell stack (V_{stack} = −15 V) along the *x*-axis at the cathode GDL-electrolyte interface (VII in Figure 7.1) in each cell for the full model and the reduced model with approximate analytical solutions. Channel Length L = 0.10 m. All the other design and operating conditions take the base case values in Table 3.1.

7.9 Table

Table 7.1. Comparison of computational time for one run of simulation of an n-cell stack with channel length 0.1 m and applied stack potential of $-3n$ V using the full model and the reduced model with approximate analytical solutions. All the other design and operating conditions take the base case values in Table 3.1.

Case	$\boldsymbol{n = 1}$	$\boldsymbol{n = 2}$	$\boldsymbol{n = 3}$	$\boldsymbol{n = 5}$
Full model solutions	15 min	37 min	176 min	489 min
Reduced model solutions	3 s	5 s	9 s	13 s

CHAPTER 8

CONCLUSIONS AND FUTURE DIRECTIONS

8.1 Summary and Conclusions

In recent years, CO_2 is widely recognized as a valuable resource, and its large-scale conversion into useful chemicals such as fuels has the potential advantages of reducing fossil fuel consumption and mitigating atmospheric CO_2 pollution. Electrochemical conversion of CO_2 into value-added chemicals offers an economically viable and sustainable route to recycle CO_2 especially when it is powered by carbon-neutral electricity source. This thesis dealt with the development of a mathematical framework for the modeling of the electrochemical reductions of CO_2 to CO in microfluidic reactors. This work was the first to present a complete mathematical modeling framework for such a system: from a detailed unit cell model, to a reduced unit cell model and subsequently to a cell stack model. It differed from prior research in one of the following ways: (1) the system used – a microfluidic flow cell while others considered other electrolyzers with a separator or membrane or solid oxide button cell; (2) the chemistry involved – the reduction of CO_2 to CO while others considered the electrolysis of water or oxidation of fuels; and (3) the complexity of the model – a 2D mathematical model accounting for the conservation of mass, momentum and charge not only in a unit cell but also in a cell stack while others considered crude cathode model or 1D elementary reaction model or only unit cell model.

In the first study as described in Chapter 3 of the thesis, a steady state and isothermal computational fluidic dynamics (CFD) model was developed to account for the transport of species and charge, conservation of mass, momentum and charge, and electrochemical reaction kinetics in a single microfluidic cell. The development of a unit cell mathematical

model was highly complicated and challenging, as it required to solve for the coupled partial differential equations that describe the multiple physical phenomena, and to resolve the geometry in different length scales varying from the catalyst layer thickness of O (10^{-6} – 10^{-4}) m to the cell length of O (10^{0} – 10^{1}) m. Electrochemical reaction kinetic parameters in the model were then calibrated and the model was validated using independent sets of experimental data. As reported in Chapter 4, the developed model agreed with the experimental data, especially at high applied cell potential of around −3 V where the cell is usually operated. With confidence on the developed model, parametric studies for several design and operating conditions on the performance of the microfluidic cell were performed using numerical simulations.

As the detailed model developed consists of a system of highly coupled partial differential equations, numerical solutions of the model will be computationally expensive, especially when a large number of the cells are stacked together to give a practical throughput of CO_2 conversion. As presented in Chapter 6, model reduction based on scaling arguments was first conducted to derive a reduced model that is significantly reduced in mathematical complexity yet preserves geometry and leading order physics. Further mathematical approximations such as Taylor series expansion and Finite Fourier Transform were employed to successfully secure approximate analytical solutions for the reduced model. This approach of model reduction was efficient as no state-space model was required, but very challenging as a thorough understanding of the system was necessary.

As demonstrated in Chapter 7, the unit cell models were further extended to cell stack models. The extension from unit cell model to cell stack model was not trivial, as the complexity of the model increased tremendously when the cell stack model was considered – additional physics and additional length scales. The reduced model with approximate

analytical solutions, as verified with the numerical solutions of the full model, are capable of capturing leading order physics even when the cell-stack is operated with a non-uniform feed flow.

8.2 Future Directions

With the developed mathematical modeling framework, the next possible phase of study is to employ the models developed to perform system design and/or process optimization. A small system comprised of a microfluidic cell stack, heat exchangers, compressors and gas separation unit can be considered. Decision variables such as the cell dimensions, number of cells in the stack, applied cell potentials, CO_2 concentration in the feed to the microfluidic cell stack can be selected to address the problem of maximizing the revenue of processing a flue gas stream with a constant flow rate and fixed compositions in a given time frame. On the next step, when the CO_2 electrolysis system is attached to a power plant which generates electricity using a renewable source and supplies electricity to the CO_2 electrolysis system at an intermittent rate, process optimization to address the scheduling problem can be another area of research interest. Economic feasibility of large scale conversion of CO_2 using such a system can also be evaluated. Additional sensitivity analysis of combination of parameters can also be performed.

Optimal nominal solutions might not be enough for a cell stack design to go into mass production, because the actual cell properties can deviate from the designed nominal value in high volume manufacturing processes. Therefore, a statistical approach such as Monte Carlo simulation can be used to correlate the variability of design and operating parameters with the global and local performance of a microfluidic cell stack, just like in the case of fuel cell stacks[120, 121]. Our approximate analytical solutions, once symbolically solved, can perform further simulation at a very low computational cost. It is also capable of capturing

the leading order physics of the microfluidic cell even when the cell is operated with some perturbation, and thus can be employed with high confidence for such Monte Carlo simulation.

In order to explore the feasibility of large scale processing of CO_2 using the CO_2 electrolysis unit, in addition to optimizing the economic return, the multi-criteria optimization of economic, environmental and social aspects, i.e. sustainable process design, of this process will be another branch of study. Sustainable process design involves the integration of life cycle assessment (LCA) which accounts for all the possible upstream and downstream environmental impacts of the raw materials, processes and products throughout the life cycle of the project, and can provide a holistic view of the environmental and technical process engineering at the early state of process design.[122-124] As an initial start, the current isothermal model be extended to a non-isothermal model by including energy balances. Subsequently, energy and exergy analysis of the system comprised of a CO_2 electrolyzer stack, heat exchangers, compressors, gas separation units and a power plant can be conducted.

BIBLIOGRAPHY

1. Administration, E.I., *International Energy Outlook 2013 With Projections to 2040*. 2013: Government Printing Office.

2. Le Quéré, C., et al., *Global carbon budget 2013.* Earth Syst. Sci. Data Discuss., 2013. **6**(2): p. 689-760.

3. Lackner, K.S., *CARBONATE CHEMISTRY FOR SEQUESTERING FOSSIL CARBON.* Annual Review of Energy and the Environment, 2002. **27**(1): p. 193-232.

4. Centi, G. and S. Perathoner, *Opportunities and prospects in the chemical recycling of carbon dioxide to fuels.* Catalysis Today, 2009. **148**(3–4): p. 191-205.

5. Plasynski, S.I., et al., *Progress and New Developments in Carbon Capture and Storage.* Critical Reviews in Plant Sciences, 2009. **28**(3): p. 123-138.

6. *Gateway to the UN System's Work on Climate Change*. 2013; Available from: http://www.un.org/wcm/content/site/climatechange/pages/gateway/mitigation.

7. Metz, B. and I.P.o.C.C.W.G. III., *Carbon Dioxide Capture and Storage: Special Report of the Intergovernmental Panel on Climate Change*. 2005: Cambridge University Press.

8. Thomas, D.C. and S.M. Benson, *Carbon Dioxide Capture for Storage in Deep Geologic Formations - Results from the CO2 Capture Project: Vol 1 - Capture and Separation of Carbon Dioxide from Combustion, Vol 2 - Geologic Storage of Carbon Dioxide with Monitoring and Verification*. 2005: Elsevier Science.

9. Taheri Najafabadi, A., *CO2chemical conversion to useful products: An engineering insight to the latest advances toward sustainability.* International Journal of Energy Research, 2013. **37**(6): p. 485-499.

10. Orr, J.F.M., *CO2 capture and storage: are we ready?* Energy & Environmental Science, 2009. **2**(5): p. 449.

11. Bachu, S. and M.A. Celia, *Assessing the potential for CO2 leakage, particularly through wells, from geological storage sites*, in *Carbon Sequestration and Its Role in the Global Carbon Cycle*. 2009, American Geophysical Union. p. 203-216.

12. Budzianowski, W.M., *Value-added carbon management technologies for low CO2 intensive carbon-based energy vectors.* Energy, 2012. **41**(1): p. 280-297.

13. Markewitz, P., et al., *Worldwide innovations in the development of carbon capture technologies and the utilization of CO2.* Energy & Environmental Science, 2012. **5**(6): p. 7281.

14. Chueh, W.C., et al., *High-Flux Solar-Driven Thermochemical Dissociation of CO2 and H2O Using Nonstoichiometric Ceria.* Science, 2010. **330**(6012): p. 1797-1801.

15. Furler, P., et al., *Solar Thermochemical CO2Splitting Utilizing a Reticulated Porous Ceria Redox System.* Energy & Fuels, 2012: p. 121024073702001.

16. Izumi, Y., *Recent advances in the photocatalytic conversion of carbon dioxide to fuels with water and/or hydrogen using solar energy and beyond.* Coordination Chemistry Reviews, 2013. **257**(1): p. 171-186.

17. Lo, C.-C., et al., *Photoreduction of carbon dioxide with H2 and H2O over TiO2 and ZrO2 in a circulated photocatalytic reactor*. Solar Energy Materials and Solar Cells, 2007. **91**(19): p. 1765-1774.

18. Hou, W., et al., *Photocatalytic Conversion of CO2to Hydrocarbon Fuels via Plasmon-Enhanced Absorption and Metallic Interband Transitions.* ACS Catalysis, 2011. **1**(8): p. 929-936.

19. Whipple, D.T., E.C. Finke, and P.J.A. Kenis, *Microfluidic Reactor for the Electrochemical Reduction of Carbon Dioxide: The Effect of pH.* Electrochemical and Solid-State Letters, 2010. **13**(9): p. B109.

20. Jhong, H.-R.M., S. Ma, and P.J.A. Kenis, *Electrochemical conversion of CO2 to useful chemicals: current status, remaining challenges, and future opportunities.* Current Opinion in Chemical Engineering, 2013. **2**(2): p. 191-199.

21. Lim, R.J., et al., *A review on the electrochemical reduction of CO2 in fuel cells, metal electrodes and molecular catalysts.* Catalysis Today, 2013.

22. Agarwal, A.S., et al., *The electrochemical reduction of carbon dioxide to formate/formic acid: engineering and economic feasibility.* ChemSusChem, 2011. **4**(9): p. 1301-10.

23. Hori, Y., et al., *Electrocatalytic process of CO selectivity in electrochemical reduction of CO2 at metal electrodes in aqueous media.* Electrochimica Acta, 1994. **39**(11–12): p. 1833-1839.

24. Stevens, G.B., T. Reda, and B. Raguse, *Energy storage by the electrochemical reduction of CO2 to CO at a porous Au film.* Journal of Electroanalytical Chemistry, 2002. **526**(1–2): p. 125-133.

25. Shi, J., et al., *A Novel Electrolysis Cell for CO2 Reduction to CO in Ionic Liquid/Organic Solvent Electrolyte.* Journal of Power Sources, 2014.

26. Yamamoto, T., et al., *Production of syngas plus oxygen from CO2 in a gas-diffusion electrode-based electrolytic cell.* Electrochimica Acta, 2002. **47**(20): p. 3327-3334.

27. Kaneco, S., et al., *Electrochemical conversion of carbon dioxide to formic acid on Pb in KOH/methanol electrolyte at ambient temperature and pressure.* Energy, 1998. **23**(12): p. 1107-1112.

28. Mahmood, M.N., D. Masheder, and C.J. Harty, *Use of gas-diffusion electrodes for high-rate electrochemical reduction of carbon dioxide. I. Reduction at lead, indium- and tin-impregnated electrodes.* Journal of Applied Electrochemistry, 1987. **17**(6): p. 1159-1170.

29. Furuya, N., T. Yamazaki, and M. Shibata, *High performance Ru□Pd catalysts for CO2 reduction at gas-diffusion electrodes.* Journal of Electroanalytical Chemistry, 1997. **431**(1): p. 39-41.

30. Cook, R.L., R.C. MacDuff, and A.F. Sammells, *High Rate Gas Phase CO 2 Reduction to Ethylene and Methane Using Gas Diffusion Electrodes.* Journal of The Electrochemical Society, 1990. **137**(2): p. 607-608.

31. Kaneco, S., et al., *Electrochemical Reduction of CO2 to Methane at the Cu Electrode in Methanol with Sodium Supporting Salts and Its Comparison with Other Alkaline Salts.* Energy & Fuels, 2005. **20**(1): p. 409-414.

32. Kaneco, S., et al., *Electrochemical conversion of carbon dioxide to methane in aqueous NaHCO3 solution at less than 273 K.* Electrochimica Acta, 2002. **48**(1): p. 51-55.

33. Kaneco, S., et al., *Electrochemical reduction of carbon dioxide to ethylene with high Faradaic efficiency at a Cu electrode in CsOH/methanol.* Electrochimica Acta, 1999. **44**(26): p. 4701-4706.

34. Kaneco, S., et al., *Electrochemical reduction of carbon dioxide to ethylene at a copper electrode in methanol using potassium hydroxide and rubidium hydroxide supporting electrolytes.* Electrochimica Acta, 2006. **51**(16): p. 3316-3321.

35. Yano, H., et al., *Selective electrochemical reduction of CO2 to ethylene at a three-phase interface on copper(I) halide-confined Cu-mesh electrodes in acidic solutions of potassium halides.* Journal of Electroanalytical Chemistry, 2004. **565**(2): p. 287-293.

36. Yano, J., et al., *Selective ethylene formation by pulse-mode electrochemical reduction of carbon dioxide using copper and copper-oxide electrodes.* Journal of Solid State Electrochemistry, 2006. **11**(4): p. 554-557.

37. Ogura, K., *Electrochemical reduction of carbon dioxide to ethylene: Mechanistic approach.* Journal of CO2 Utilization, 2013. **1**(0): p. 43-49.

38. Ganesh, I., *Conversion of carbon dioxide into methanol – a potential liquid fuel: Fundamental challenges and opportunities (a review).* Renewable and Sustainable Energy Reviews, 2014. **31**: p. 221-257.

39. Summers, D.P., S. Leach, and K.W. Frese Jr, *The electrochemical reduction of aqueous carbon dioxide to methanol at molybdenum electrodes with low overpotentials.* Journal of Electroanalytical Chemistry and Interfacial Electrochemistry, 1986. **205**(1–2): p. 219-232.

40. Jia, F., X. Yu, and L. Zhang, *Enhanced selectivity for the electrochemical reduction of CO2 to alcohols in aqueous solution with nanostructured Cu–Au alloy as catalyst.* Journal of Power Sources, 2014. **252**(0): p. 85-89.

41. Kuhl, K.P., et al., *New insights into the electrochemical reduction of carbon dioxide on metallic copper surfaces.* Energy & Environmental Science, 2012. **5**(5): p. 7050.

42. Gattrell, M., N. Gupta, and A. Co, *A review of the aqueous electrochemical reduction of CO2 to hydrocarbons at copper*. Journal of Electroanalytical Chemistry, 2006. **594**(1): p. 1-19.

43. Li, H. and C. Oloman, *Development of a continuous reactor for the electro-reduction of carbon dioxide to formate – Part 1: Process variables.* Journal of Applied Electrochemistry, 2006. **36**(10): p. 1105-1115.

44. Thorson, M.R., K.I. Siil, and P.J.A. Kenis, *Effect of Cations on the Electrochemical Conversion of CO2 to CO.* Journal of the Electrochemical Society, 2012. **160**(1): p. F69-F74.

45. Rosen, B.A., et al., *Ionic liquid-mediated selective conversion of CO(2) to CO at low overpotentials.* Science, 2011. **334**(6056): p. 643-4.

46. Tornow, C.E., et al., *Nitrogen-Based Catalysts for the Electrochemical Reduction of CO2 to CO.* Journal of the American Chemical Society, 2012. **134**(48): p. 19520-19523.

47. Benson, E.E., et al., *Electrocatalytic and homogeneous approaches to conversion of CO2 to liquid fuels.* Chem Soc Rev, 2009. **38**(1): p. 89-99.

48. Thorson, M.R., *Using microscale flow cells to study the electrochemical reduction of carbon dioxide*. 2012, University of Illinois at Urbana-Champaign.

49. Jensen, S.H., et al., *Hydrogen and synthetic fuel production using pressurized solid oxide electrolysis cells.* International Journal of Hydrogen Energy, 2010. **35**(18): p. 9544-9549.

50. Delacourt, C., et al., *Design of an Electrochemical Cell Making Syngas (CO+H[sub 2]) from CO[sub 2] and H[sub 2]O Reduction at Room Temperature.* Journal of The Electrochemical Society, 2008. **155**(1): p. B42.

51. Bidrawn, F., et al., *Efficient Reduction of CO[sub 2] in a Solid Oxide Electrolyzer.* Electrochemical and Solid-State Letters, 2008. **11**(9): p. B167.

52. Uhm, S. and Y.D. Kim, *Electrochemical conversion of carbon dioxide in a solid oxide electrolysis cell.* Current Applied Physics, 2014. **14**(5): p. 672-679.

53. Hori, Y., *Electrochemical CO2 Reduction on Metal Electrodes*, in *Modern Aspects of Electrochemistry*, C. Vayenas, R. White, and M. Gamboa-Aldeco, Editors. 2008, Springer New York. p. 89-189.

54. Azuma, M., et al., *Electrochemical Reduction of Carbon Dioxide on Various Metal Electrodes in Low-Temperature Aqueous KHCO 3 Media.* Journal of The Electrochemical Society, 1990. **137**(6): p. 1772-1778.

55. Jitaru, M., et al., *Electrochemical reduction of carbon dioxide on flat metallic cathodes.* Journal of Applied Electrochemistry, 1997. **27**(8): p. 875-889.

56. Chen, Y. and M.W. Kanan, *Tin Oxide Dependence of the CO2 Reduction Efficiency on Tin Electrodes and Enhanced Activity for Tin/Tin Oxide Thin-Film Catalysts.* Journal of the American Chemical Society, 2012. **134**(4): p. 1986-1989.

57. Hinogami, R., et al., *Electrochemical Reduction of Carbon Dioxide Using a Copper Rubeanate Metal Organic Framework.* ECS Electrochemistry Letters, 2012. **1**(4): p. H17-H19.

58. Hori, Y., *CO2-reduction, catalyzed by metal electrodes*, in *Handbook of Fuel Cells*. 2010, John Wiley & Sons, Ltd.

59. Li, H. and C. Oloman, *Development of a continuous reactor for the electro-reduction of carbon dioxide to formate – Part 2: Scale-up.* Journal of Applied Electrochemistry, 2007. **37**(10): p. 1107-1117.

60. Delacourt, C., P.L. Ridgway, and J. Newman, *Mathematical Modeling of CO[sub 2] Reduction to CO in Aqueous Electrolytes.* Journal of The Electrochemical Society, 2010. **157**(12): p. B1902.

61. Shi, Y., et al., *Experimental characterization and modeling of the electrochemical reduction of CO2 in solid oxide electrolysis cells.* Electrochimica Acta, 2013. **88**: p. 644-653.

62. Li, W., et al., *Elementary reaction modeling of CO2/H2O co-electrolysis cell considering effects of cathode thickness.* Journal of Power Sources, 2013. **243**: p. 118-130.

63. Li, W., et al., *Theoretical modeling of air electrode operating in SOFC mode and SOEC mode: The effects of microstructure and thickness.* International Journal of Hydrogen Energy, 2014. **39**(25): p. 13738-13750.

64. Li, W., et al., *Elementary reaction modeling of solid oxide electrolysis cells: Main zones for heterogeneous chemical/electrochemical reactions.* Journal of Power Sources, 2015. **273**: p. 1-13.

65. Li, W., et al., *Performance and methane production characteristics of H2O–CO2 co-electrolysis in solid oxide electrolysis cells.* International Journal of Hydrogen Energy, 2013. **38**(25): p. 11104-11109.

66. Luo, Y., et al., *Comprehensive modeling of tubular solid oxide electrolysis cell for co-electrolysis of steam and carbon dioxide.* Energy, 2014. **70**: p. 420-434.

67. Zhang, J., Y. Shi, and N. Cai, *An approximate analytical model of reduction of carbon dioxide in solid oxide electrolysis cell by regular and singular perturbation methods.* Electrochimica Acta, 2014. **139**: p. 190-200.

68. Ni, M., *Modeling of a solid oxide electrolysis cell for carbon dioxide electrolysis.* Chemical Engineering Journal, 2010. **164**(1): p. 246-254.

69. Ni, M., *An electrochemical model for syngas production by co-electrolysis of H2O and CO2.* Journal of Power Sources, 2012. **202**: p. 209-216.

70. Ni, M., *2D thermal modeling of a solid oxide electrolyzer cell (SOEC) for syngas production by H2O/CO2 co-electrolysis.* International Journal of Hydrogen Energy, 2012. **37**(8): p. 6389-6399.

71. Xie, Y. and X. Xue, *Modeling of solid oxide electrolysis cell for syngas generation with detailed surface chemistry.* Solid State Ionics, 2012. **224**: p. 64-73.

72. Narasimhaiah, G. and V.M. Janardhanan, *Modeling CO2 electrolysis in solid oxide electrolysis cell.* Journal of Solid State Electrochemistry, 2013. **17**(8): p. 2361-2370.

73. García-Camprubí, M., S. Izquierdo, and N. Fueyo, *Challenges in the electrochemical modelling of solid oxide fuel and electrolyser cells.* Renewable and Sustainable Energy Reviews, 2014. **33**: p. 701-718.

74. Stempien, J.P., et al., *Energy and exergy analysis of Solid Oxide Electrolyser Cell (SOEC) working as a CO2 mitigation device.* International Journal of Hydrogen Energy, 2012. **37**(19): p. 14518-14527.

75. Stempien, J.P., Q. Sun, and S.H. Chan, *Performance of power generation extension system based on solid-oxide electrolyzer cells under various design conditions.* Energy, 2013. **55**: p. 647-657.

76. Bazylak, A., D. Sinton, and N. Djilali, *Improved fuel utilization in microfluidic fuel cells: A computational study.* Journal of Power Sources, 2005. **143**(1-2): p. 57-66.

77. Chang, M.-H., F. Chen, and N.-S. Fang, *Analysis of membraneless fuel cell using laminar flow in a Y-shaped microchannel.* Journal of Power Sources, 2006. **159**(2): p. 810-816.

78. Chen, F., M.-H. Chang, and M.-K. Lin, *Analysis of membraneless formic acid microfuel cell using a planar microchannel.* Electrochimica Acta, 2007. **52**(7): p. 2506-2514.

79. Chen, W. and F. Chen, *Theoretical approaches to studying the single and simultaneous reactions in laminar flow-based membraneless fuel cells.* Journal of Power Sources, 2006. **162**(2): p. 1137-1146.

80. Chen, F., M.-H. Chang, and C.-W. Hsu, *Analysis of membraneless microfuel cell using decomposition of hydrogen peroxide in a Y-shaped microchannel.* Electrochimica Acta, 2007. **52**(25): p. 7270-7277.

81. Ahmed, D.H., H.B. Park, and H.J. Sung, *Optimum geometrical design for improved fuel utilization in membraneless micro fuel cell.* Journal of Power Sources, 2008. **185**(1): p. 143-152.

82. Wang, X.-Q., et al., *Flow and thermal characteristics of offset branching network.* International Journal of Thermal Sciences, 2010. **49**(2): p. 272-280.

83. Ebrahimi Khabbazi, A., A.J. Richards, and M. Hoorfar, *Numerical study of the effect of the channel and electrode geometry on the performance of microfluidic fuel cells.* Journal of Power Sources, 2010. **195**(24): p. 8141-8151.

84. Krishnamurthy, D., et al., *Computational modeling of microfluidic fuel cells with flow-through porous electrodes.* Journal of Power Sources, 2011. **196**(23): p. 10019-10031.

85. Shaegh, S.A.M., N.-T. Nguyen, and S.H. Chan, *An air-breathing microfluidic formic acid fuel cell with a porous planar anode: experimental and numerical investigations.* Journal of Micromechanics and Microengineering, 2010. **20**(10): p. 105008.

86. Xuan, J., et al., *A computational study of bifunctional oxygen electrode in air-breathing reversible microfluidic fuel cells.* International Journal of Hydrogen Energy, 2011. **36**(15): p. 9231-9241.

87. Wang, H., D.Y.C. Leung, and J. Xuan, *Modeling of an air cathode for microfluidic fuel cells: Transport and polarization behaviors.* International Journal of Hydrogen Energy, 2011. **36**(22): p. 14704-14718.

88. Xuan, J., et al., *Theoretical Graetz–Damköhler modeling of an air-breathing microfluidic fuel cell.* Journal of Power Sources, 2013. **231**: p. 1-5.

89. García-Cuevas, R.A., et al., *Toward geometrical design improvement of membraneless fuel cells: Numerical study.* International Journal of Hydrogen Energy, 2013. **38**(34): p. 14791-14800.

90. Zhang, B., et al., *Computational modeling of air-breathing microfluidic fuel cells with flow-over and flow-through anodes.* Journal of Power Sources, 2014. **259**: p. 15-24.

91. Yu, Y., et al., *A Hierarchical Multiscale Model for Microfluidic Fuel Cells with Porous Electrodes.* Electrochimica Acta, 2014. **116**: p. 237-243.

92. Moein-Jahromi, M., S. Movahed, and M.J. Kermani, *Numerical study of the cathode electrode in the Microfluidic Fuel Cell using agglomerate model.* Journal of Power Sources, 2015. **277**: p. 180-192.

93. Bosch, P.P.J.v.d. and A.C.v.d. Klauw, *Modeling, identification, and simulation of dynamical systems*. 1994, Boca Raton: CRC Press.

94. Um, S., C.Y. Wang, and K.S. Chen, *Computational Fluid Dynamics Modeling of Proton Exchange Membrane Fuel Cells.* Journal of The Electrochemical Society, 2000. **147**(12): p. 4485-4493.

95. Birgersson, E., M. Noponen, and M. Vynnycky, *Analysis of a Two-Phase Non-Isothermal Model for a PEFC.* Journal of The Electrochemical Society, 2005. **152**(5): p. A1021.

96. Ubong, E.U., Z. Shi, and X. Wang, *Three-Dimensional Modeling and Experimental Study of a High Temperature PBI-Based PEM Fuel Cell.* Journal of The Electrochemical Society, 2009. **156**(10): p. B1276.

97. Curtiss, C.F. and R.B. Bird, *Multicomponent Diffusion.* Industrial & Engineering Chemistry Research, 1999. **38**(7): p. 2515-2522.

98. Cussler, E.L., *Multicomponent Diffusion*. 1976: Elsevier Scientific Publishing Company.

99. Cussler, E.L., *Diffusion: Mass Transfer in Fluid Systems*. 3rd ed. 2009: Cambridge University Press.

100. Fuller, E.N., P.D. Schettler, and J.C. Giddings, *NEW METHOD FOR PREDICTION OF BINARY GAS-PHASE DIFFUSION COEFFICIENTS.* Industrial & Engineering Chemistry, 1966. **58**(5): p. 18-27.

101. Tomadakis, M.M., *Viscous Permeability of Random Fiber Structures: Comparison of Electrical and Diffusional Estimates with Experimental and Analytical Results.* Journal of Composite Materials, 2005. **39**(2): p. 163-188.

102. Jhong, H.R., et al., *Combining Structural and Electrochemical Analysis of Electrodes Using Micro-Computed Tomography and a Microfluidic Fuel Cell.* Journal of the Electrochemical Society, 2012. **159**(3): p. B292-B298.

103. Ma, L., D.B. Ingham, and M.C. Pourkashanian, *16 - Application of fluid flows through porous media in fuel cells*, in *Transport Phenomena in Porous Media III*, D.B. Ingham and I. Pop, Editors. 2005, Pergamon: Oxford. p. 418-440.

104. Whipple, D.T., *Microfluidic Platform for Studying the Electrochemical Reduction of Carbon Dioxide*, in *Chemical Engineering*. 2011, University of Illinois at Urbana-Champaign: Urbana, Illinois.

105. COMSOL. *COMSOL Multiphysics*. Available from: http://www.comsol.com/.

106. Welty, J.R., et al., *Fundamentals of momentum, heat, and mass transfer*. 2009: John Wiley & Sons.

107. Newman, J. and K.E. Thomas-Alyea, *Electrochemical Systems*. 3rd ed. 2004.

108. Perry, R.H. and D.W. Green, *Perry's chemical engineers' handbook*. 2008, New York: McGraw-Hill.

109. Mathworks. *MATLAB*. Available from: http://www.mathworks.com.

110. Björkman, M. and K. Holmström *Global optimization using DIRECT algorithm in matlab.* Advanced Modeling and Optimization, 1999. **1**(2).

111. Krantz, W.B., *Introduction*, in *Scaling Analysis in Modeling Transport and Reaction Processes*. 2006, John Wiley & Sons, Inc. p. 1-6.

112. Ee, S.L. and E. Birgersson, *Two-Dimensional Approximate Analytical Solutions for the Anode of a Direct Methanol Fuel Cell.* Journal of The Electrochemical Society, 2009. **156**(11): p. B1329.

113. Ee, S.L. and E. Birgersson, *Two-Dimensional Approximate Analytical Solutions for the Direct Liquid Fuel Cell.* Journal of The Electrochemical Society, 2011. **158**(10): p. B1224.

114. Vynnycky, M. and E. Birgersson, *Analysis of a Model for Multicomponent Mass Transfer in the Cathode of a Polymer Electrolyte Fuel Cell.* SIAM Journal on Applied Mathematics, 2003. **63**(4): p. 1392-1423.

115. Birgersson, E., et al., *Reduced Two-Dimensional One-Phase Model for Analysis of the Anode of a DMFC.* Journal of The Electrochemical Society, 2003. **150**(10): p. A1368.

116. Maplesoft. *Maple*. Available from: http://www.maplesoft.com/products/.

117. Chang, P.A.C., et al., *Flow distribution in proton exchange membrane fuel cell stacks.* Journal of Power Sources, 2006. **162**(1): p. 340-355.

118. Chen, C.-H., S.-P. Jung, and S.-C. Yen, *Flow distribution in the manifold of PEM fuel cell stack.* Journal of Power Sources, 2007. **173**(1): p. 249-263.

119. Ly, H., E. Birgersson, and M. Vynnycky, *Asymptotically Reduced Model for a Proton Exchange Membrane Fuel Cell Stack: Automated Model Generation and Verification.* Journal of The Electrochemical Society, 2010. **157**(7): p. B982.

120. He, Z., H. Li, and E. Birgersson, *Correlating variability of modeling parameters with non-isothermal stack performance: Monte Carlo simulation of a portable 3D planar solid oxide fuel cell stack.* Applied Energy, 2014. **136**: p. 560-575.

121. Cornu, T.M. and Z. Wuillemin, *Impact of Random Geometric Distortions on the Performance and Reliability of an SOFC.* Fuel Cells, 2011. **11**(4): p. 553-564.

122. Chang, D., C.K.M. Lee, and C.-H. Chen, *Review of life cycle assessment towards sustainable product development.* Journal of Cleaner Production, 2014. **83**: p. 48-60.

123. Bakshi, B.R., *Methods and tools for sustainable process design.* Current Opinion in Chemical Engineering, 2014. **6**: p. 69-74.

124. Fazeni, K., J. Lindorfer, and H. Prammer, *Methodological advancements in Life Cycle Process Design: A preliminary outlook.* Resources, Conservation and Recycling, 2014. **92**: p. 66-77.